Defence Research and Development Canada
Recherche et développement pour la défense Canada

DRDC | RDDC

Experimental verification of multiple-input multiple output (MIMO) beamforming capabilities using a time-division coherent MIMO radar

P. Sévigny
P.W. Moo
T. Laneve

Defence Research and Development Canada

Scientific Report
DRDC-RDDC-2015-R051
April 2015

Canada

Experimental verification of multiple-input multiple output (MIMO) beamforming capabilities using a time-division coherent MIMO radar

P. Sévigny
P.W. Moo
T. Laneve

Defence Research and Development Canada
Scientific Report
DRDC-RDDC-2015-R051
April 2015

Abstract

Recently, there has been increasing interest from the research community in multiple-input multiple output (MIMO) architectures for a variety of radar applications. We are interested in clarifying the angle estimation accuracy of coherent or co-located MIMO radar to gain an accurate understanding of its potential benefits. The theoretical two-way antenna radiation patterns are derived for three configurations of a linear array: a phased array configuration, a MIMO-1 configuration using orthogonal waveform transmission on all elements, and a MIMO-2 configuration using orthogonal waveform transmission on the two end elements. Field experimental results obtained with an 8-element X-band linear array time-division radar and trihedral targets are discussed. Phased array radar data obtained with a Mixed Experiments and Simulations Approach (MESA) are also discussed. It is found that the experimental mainbeam patterns match the theoretical patterns. MIMO-1 is shown to have the same two-way radiation pattern as that of a phased array radar configuration. Compared to MIMO-1 and phased array, MIMO-2 has enhanced angle estimation accuracy, lower gain and higher sidelobes, while only requiring two orthogonal waveforms on transmit.

Significance for defence and security

Multiple-input multiple output (MIMO) radars have a number of potential benefits and may represent a future evolution of current phased array radars. The results discussed in this report, obtained with an 8-channel X-band linear array time-division MIMO radar, clarify the angle estimation accuracy of coherent MIMO radar. This understanding is crucial in the development of MIMO radar signal processing algorithms and applications.

Résumé

Récemment, nous avons observé un intérêt accru de la part de la communauté de la recherche pour les architectures à entrées multiples, sorties multiples (MIMO) pour une variété d'applications radars. Nous voulons clarifier l'exactitude de l'estimation de l'angle des radars MIMO cohérents ou co-localisés, pour obtenir une compréhension précise de leurs bénéfices potentiels. Le diagramme de rayonnement de l'antenne bidirectionnel théorique est dérivé pour trois configurations d'un réseau linéaire : une configuration avec une antenne à réseau à éléments en phase, une configuration MIMO-1 qui utilise la transmission de formes d'onde orthogonales pour tous les éléments, et une configuration MIMO-2 qui utilise la transmission de formes d'ondes orthogonales aux deux éléments des extrémités. Des résultats expérimentaux obtenus sur le terrain avec un radar de bande X à 8 canaux et à répartition dans le temps sont discutés. Des données de radar à réseau à éléments en phase, obtenus avec une approche mixte d'expérimentations et de simulations (MESA), sont également discutés. On y trouve que les faisceaux principaux des diagrammes de rayonnement expérimentaux concordent avec ceux des diagrammes théoriques. On y montre que MIMO-1 a le même diagramme de rayonnement bidirectionel que la configuration radar à réseau à éléments en phase. En comparaison de MIMO-1 et du radar à réseau à éléments en phase, MIMO-2 a une exactitude accrue de l'estimation de l'angle, un gain d'antenne plus faible et des lobes secondaires plus importants, par contre il ne nécessite que deux formes d'ondes orthogonales pour la transmission.

Importance pour la défense et la sécurité

Les bénéfices potentiels des radars à entrées multiples, sorties multiples (MIMO) sont nombreux et ces derniers pourraient représenter l'évolution future des radars à réseau à éléments en phase actuels. Les résultats discutés dans ce rapport, obtenus avec un radar MIMO de bande X à 8 canaux et à répartition dans le temps, clarifient l'exactitude de l'estimation de l'angle des radars MIMO cohérents. Cette compréhension est cruciale pour le développement des algorithmes de traitement des signaux des radars MIMO et leurs applications.

Acknowledgements

The authors would like to thank Pietro Reitano for his contribution to the data collection and Agilent for the lease of the VNA.

This page intentionally left blank.

Table of contents

List of figures

List of tables

This page intentionally left blank.

1 Introduction

Recently, there has been increasing interest from the research community in multiple-input multiple output (MIMO) architectures for a variety of radar applications [1, 2, 3]. The MIMO concept was first developed for communications systems, for which orthogonal transmit-receive channels are used to circumvent channel fading [4]. In the field of radar, widely separated antenna MIMO radars exploit spatial diversity, while co-located or coherent MIMO radars use multiple transmit waveforms to obtain further degrees of freedom and improve radar performance. See [5] and [6] for a comprehensive literature survey of MIMO radar. In this work, attention is focused on coherent MIMO radar, which requires the use of orthogonal waveforms on transmit and increased signal processing on receive, and therefore has increased complexity and flexibility compared to phased array operation.

Coherent MIMO radar has a number of potential benefits, including the use of omni-directional search modes [7], enhanced clutter cancellation [8], and increased Doppler resolution [9]. Because of the increased complexity of MIMO radar, it is important to gain an accurate understanding of its potential benefits. In particular, it has been previously stated that MIMO radar has enhanced angle estimation accuracy compared to phased array radar. This increased accuracy results from an apparent decrease in antenna beamwidth when the linear array is operated as a MIMO radar [10, 11, 12, 13, 14].

In this paper, we are interested in clarifying this statement about the enhanced angle estimation accuracy. The mathematical formulation to support our analysis is provided in Section 2. We then provide simple but yet conclusive experimental results to support our analysis. The experimental methodology is described in Section 3 and the results are presented in Section 4. A discussion and conclusions are provided in Section 5.

2 Theoretical antenna patterns

Two-way antenna radiation patterns are derived for an N-element linear array, for uniform phase and magnitude illumination, operating in three distinct configurations: Phased Array, MIMO-1, and MIMO-2. In the Phased Array configuration, a single waveform is transmitted coherently across the array, and the return is received coherently on all elements. For the MIMO-1 configuration, each element transmits a distinct orthogonal waveform, and the return is received coherently on all elements. For the MIMO-2 configuration, each of the end elements transmits a distinct orthogonal waveform, and the return is received coherently on the first $N-1$ elements. See Figure 1 for an illustration of the configurations. Each element in the array has element factor $E(\theta)$, where θ is the azimuth angle. A linear array with N elements has a normalized power array factor $A_N(\theta)$, given by

$$A_N(\theta) = \frac{\sin^2[N\pi(d/\lambda)\sin\theta]}{N^2\,\sin^2[\pi(d/\lambda)\sin\theta]}, \tag{1}$$

where d is the inter-element spacing, and λ is the wavelength. The array factor, for narrow-band and far-field approximations, can be derived by summing the vector contributions from all elements, i.e.

$$\begin{aligned} A_N(\theta) &= \left|\frac{1}{\sqrt{N}}\sum_{n=0}^{N-1} e^{j\frac{2\pi c}{\lambda}\tau_n}\right|^2 && (2)\\ &= \left|\frac{1}{\sqrt{N}}\sum_{n=0}^{N-1} e^{j\frac{2\pi}{\lambda}nd\sin\theta}\right|^2, && (3)\end{aligned}$$

where τ_n is the travel time between a point target and the nth element of the array.

2.1 Phased Array configuration

For the Phased Array configuration, the transmit radiation pattern $G_{\mathrm{PA,Tx}}(\theta)$ and the receive radiation pattern $G_{\mathrm{PA,Rx}}(\theta)$ are equal, so that [15]

$$G_{\mathrm{PA,Tx}}(\theta) = G_{\mathrm{PA,Rx}}(\theta) = E(\theta)\,A_N(\theta).$$

The Phased Array two-way radiation pattern $G_{\mathrm{PA,2-way}}(\theta)$ is given by

$$G_{\mathrm{PA,2-way}}(\theta) = G_{\mathrm{PA,Tx}}(\theta)\,G_{\mathrm{PA,Rx}}(\theta) = E(\theta)^2\,A_N(\theta)^2. \tag{4}$$

2.2 MIMO-1 configuration

The signal model for MIMO operation, for which M orthogonal waveforms are transmitted with uniform amplitude and are received at each of N receive elements, for a

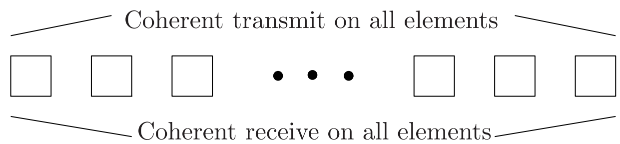

(a) *Phased Array*

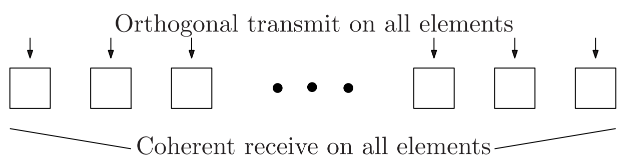

(b) *MIMO-1*

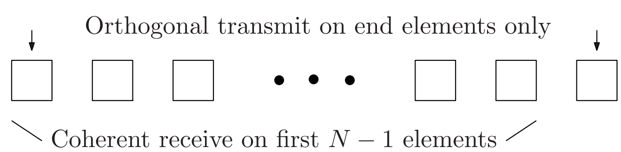

(c) *MIMO-2*

Figure 1: *Configurations for a linear array radar.*

total of MN matched filters and MN received signals, is of the form:

$$\begin{aligned} S &= \left| \frac{1}{\sqrt{MN}} \sum_{m=0}^{M-1} \sum_{n=0}^{N-1} e^{j\frac{2\pi c}{\lambda}(\tau_m+\tau_n)} \right|^2 && (5) \\ &= \left| \frac{1}{\sqrt{M}} \sum_{m=0}^{M-1} \left(\frac{1}{\sqrt{N}} \sum_{n=0}^{N-1} e^{j\frac{2\pi c}{\lambda}\tau_n} \right) e^{j\frac{2\pi c}{\lambda}\tau_m} \right|^2, && (6) \end{aligned}$$

where τ_m and τ_n are the travel times between a point target and the mth transmitter and the nth receiver, respectively. This equation reduces to

$$S = A_N(\theta)A_M(\theta) \tag{7}$$

when considering a linear array with the narrowband and far-field approximations.

This signal model applies to MIMO beamforming on receive and is equivalent to an effective receive array $TR(x)$ that is the spatial convolution of a transmit array $T(x)$ and a receive array $R(x)$ [12]. Assuming

$$\begin{aligned} T(x) &= \sum_{m=0}^{M-1} \delta(x - x_m) && (8) \\ R(x) &= \sum_{n=0}^{N-1} \delta(x - x_n), && (9) \end{aligned}$$

where x is the position across the linear array, x_m are the locations of the transmit elements and x_n are the locations of the receive elements, then the spatial convolution is the following:

$$\begin{aligned} TR(x) &= \int T(x-s)R(s)ds = \int \sum_{m=0}^{M-1} \delta(x - x_m - s) \sum_{n=0}^{N-1} \delta(s - x_n)ds && (10) \\ &= \sum_{m=0}^{M-1} \sum_{n=0}^{N-1} \int \delta(s - (x - x_m))\delta(s - x_n)ds. && (11) \end{aligned}$$

Using

$$\int \delta(s-a)f(s)ds = f(a), \tag{12}$$

then

$$\begin{aligned} TR(x) &= \sum_{m=0}^{M-1} \sum_{n=0}^{N-1} \delta\left((x - x_m) - x_n\right) && (13) \\ &= \sum_{m=0}^{M-1} \sum_{n=0}^{N-1} \delta\left(x - (x_m + x_n)\right) && (14) \end{aligned}$$

which is also a linear array with virtual elements located at $x = x_m + x_n$ for $0 \leq m \leq M-1$ and $0 \leq n \leq N-1$.

Using this signal model for the MIMO-1 configuration, the transmit radiation pattern $G_{\mathrm{M1,Tx}}(\theta)$ is given by the element pattern,

$$G_{\mathrm{M1,Tx}}(\theta) = E(\theta).$$

On receive, the effective array is the spatial convolution of the transmit linear array and the receive linear array. Therefore, the MIMO-1 receive array factor is the product of an N-element linear array factor by itself, that is, $A_N(\theta)^2$. The MIMO-1 receive radiation pattern $G_{\mathrm{M1,Rx}}(\theta)$ is then specified by

$$G_{\mathrm{M1,Rx}}(\theta) = E(\theta)\, A_N(\theta)^2.$$

The MIMO-1 two-way radiation pattern $G_{\mathrm{M1,2-way}}(\theta)$ is given by

$$G_{\mathrm{M1,2-way}}(\theta) = G_{\mathrm{M1,Tx}}(\theta)\, G_{\mathrm{M1,Rx}}(\theta) = E(\theta)^2\, A_N(\theta)^2. \tag{15}$$

The two-way radiation pattern for the MIMO-1 configuration is equal to the two-way radiation pattern for the Phased Array configuration.

2.3 MIMO-2 configuration

For the MIMO-2 configuration, the transmit radiation pattern $G_{\mathrm{M2,Tx}}(\theta)$ is given by the element pattern,

$$G_{\mathrm{M2,Tx}}(\theta) = E(\theta).$$

On receive, the effective array is the spatial convolution of the 2-element transmit linear array and the $(N-1)$-element receive linear array, i.e. a linear array with $2N-2$ elements. Therefore, the MIMO-2 receive array factor is that of a linear array with $2N-2$ elements. The MIMO-2 receive radiation pattern $G_{\mathrm{M2,Rx}}(\theta)$ is then specified by

$$G_{\mathrm{M2,Rx}}(\theta) = E(\theta)\, A_{2N-2}(\theta).$$

The MIMO-2 two-way radiation pattern $G_{\mathrm{M2,2-way}}(\theta)$ is given by

$$G_{\mathrm{M2,2-way}}(\theta) = G_{\mathrm{M2,Tx}}(\theta)\, G_{\mathrm{M2,Rx}}(\theta) = E(\theta)^2\, A_{2N-2}(\theta). \tag{16}$$

3 Experiment methodology

For the purpose of this research, a time-division 8-channel MIMO radar was developed and tested on an open field using trihedrals as targets. The targets and layout of the scenes are described in Section 3.1. The array is described in Section 3.2. The laboratory equipment assembled and used to serve as a radar is described in Section 3.3. Data was also collected using a Vector Network Analyser (VNA) to complement an Agilent ADS simulation to mimic a phased-array radar. This methodology, named Mixed Experiments and Simulations Approach (MESA), is described in Section 3.4.

3.1 Scene

The experiment was conducted in an open field, as shown in Figure 2. The array was mounted on a tripod approximately 2.35 m above the ground. One trihedral denoted PC, of 69.6 cm side, was positioned at 35 m range from the center of the array, at an angle of -4.8° off boresight in azimuth, and a height of approximately 1.7 m. This trihedral acted as a calibration target and remained in the scene for all scenarios. One or two trihedrals, both of 75 cm side, were positioned at a range of 45 m from the array center, at a height of approximately 1.6 m, except for one scene where the trihedral was lowered to a height of 1.0 m. These trihedrals were used as targets, and were positioned at various angles off boresight depending on the scenario. They are denoted as P1 to P4 in Table 1, which provides an overview of the different scenarios and the location of the targets. The far-field range of the array and of the trihedrals is 26, 29 and 34 m respectively, according to $R_{ff} = 2D^2/\lambda$ at 9.0 GHz.

Ground truth location of the targets and array for this experiment was obtained using a Leica Total Station TS15 [16].

3.2 Array

A linear array was assembled out of 10 Narda 640 horn antennae [17], as shown in Figure 3. The 8 central elements of the array are active while the two end elements are terminated to reduce edge effects. The antenna elements are positioned 8.2 cm apart and are operated at 9.0 GHz. At this frequency, grating lobes are expected every 24°.

The dimensions of the Narda 640 horn antennae are 5.954×7.859 cm, and their beamwidths are estimated to be 30° and 32° at 9.0 GHz, in the E and H planes respectively. For this experiment, vertical polarization was used.

Table 1: *List of runs for the time-division MIMO experiment.*

Filename	Description	Target(s)				
		PC	P1	P2	P3	P4
		-4.8°	-0.4°	+1.6°	+4.6°	+14.8°
		35 m	45 m	45 m	45 m	45 m
scene1	Empty scene	X				
scene5	One target at -0.4°	X	X			
scene7	One target at +1.6°	X		X		
scene3	One target at +4.6°	X			X	
scene2	One target at +4.6°, lower height	X			X	
scene9	One target at +14.8°	X				X
scene6	Two targets 2.1° apart	X	X	X		
scene4	Two targets 5.0° apart	X	X		X	
scene8	Two targets 13.2° apart	X		X		X

Figure 2: *Photograph of the experimental setup, showing the array, the smaller trihedral used as a calibration target, and the larger trihedral used as the target.*

Figure 3: *Photograph of the linear array assembled for the time-division MIMO experiment.*

3.3 Time-division 8-channel MIMO radar

3.3.1 Measurement setup

A time-division 8-channel MIMO radar was assembled using laboratory equipment as shown in Figure 4. A list of components used for the test is provided in Table 2. An Arbitrary Waveform Generator, (AWG1), produces differential I/Q signals which are routed to the wideband input ports of a Vector Signal Generator, VSG1. The VSG upconverts the base-band I/Q signal to X-band. This results in an Linear Frequency Modulated (LFM) signal centered at 9.0 GHz, with a bandwidth of 150 MHz and a pulse width of 100 μs. The chirp rate is +1.5 MHz/μs. The Tx signal is routed sequentially to each of the 8 Tx/Rx antennas via a SP10T microwave switch, SW1. The received signal is routed via SP2T switches, SW2-SW5, to the 4 channels of a digital oscilloscope, OSC1. The measurement is fully automated and uses Agilent's Signal Studio for Pulse Building (SSPB), N7620B, to generate the transmit waveform, Agilent's Vector Signal Analysis (VSA) software to demodulate, decimate, and perform data transfer of the digitized time domain data. Control of the SSPB and VSA software along with switch control and data storage is accomplished via in-house code written in Agilent's VeePro 9.3 software. The VeePro software interfaces with the SSPB and VSA software packages via .COM and .NET APIs respectively.

Prior to measurement, a calibration is performed in order to flatten the frequency response of the Tx signal. The spectrum analyzer, SA1, is connected to the ends of each of the RF cables (CAB1-8) in turn. The AWG and VSG produce a CW tone which is swept across a frequency band centered at 9.0 GHz with a bandwidth of 250 MHz. The SSPB software then uses this information to predistort the base band I/Q signals such that a flat frequency response is obtained at the antenna input. The calibrated signal for each of the 8 paths of the Tx signal are stored and applied during the measurement. During the calibration, the power at the antenna input is measured and adjusted such that it is equal for all 8 channels.

The measurement procedure involves transmitting a signal on one transmit channel, then receiving it on the 4 odd numbered receive channels simultaneously (i.e receive channels Rx1, Rx3, Rx5, and Rx7). The transmit switch, SW1, is then switched to the next transmit channel and the signal is received on the same 4 odd numbered receive channels. This procedure is repeated until the Tx signal has been transmitted through all 8 Tx channels. The receive switches, SW2-SW5, are then toggled such that the even numbered receive channels, Rx2, Rx4, Rx6, and Rx8 are now connected to OSC1 and the odd numbered Rx channels are terminated into 50 Ω. The Tx signal is now transmitted in sequence through each Tx channel (via SW1) and received on the 4 even numbered Rx channels simultaneously.

When the measurement procedure is finished, data for a complete 8×8 time division

Table 2: *List of components for the time-division MIMO experiment.*

Designator	Part	Manufacturer	Description
AD1-8	—	—	N(f) to SMA(m) adapter
AD9-12	54855-67604	Agilent	Precision BNC to 3.5 mm (f) adaptors
ANT1-ANT10	640	Narda	8-12.4 GHz Horn, No. 5
AWG1	M8190A	Agilent	Arbitrary Waveform Generator 12 Gsa/s
VSG1	E8267D	Agilent	PSG Vector Signal Generator, 20 GHz
SA1	E4440	Agilent	Performance Spectrum Analyzer (PSA)
OSC1	DSO91204A	Agilent	Digital Oscilloscope, BW = 12 GHz
CAB1-8	SF104PEA/16N/11SMA	Huber & Suhner	2.5 m rf cables
CAB9-16	MiniBend-16	Astrolab	16" rf cables
CAB17-20	MiniBend-12	Astrolab	12" rf cables
CAB21-24	MiniBend-16	Astrolab	16" rf cables
CAB25, CAB27, CAB28	EF400	Huber & Suhner	1 m BNC cable
CAB26	—	Huber & Suhner	20" BNC cable
CAB29	—	—	GPIB cable
CAB30	—	—	GPIB cable
CAB31	EF400	Huber & Suhner	2 m BNC cable
CIR1-CIR8	ESC0950	Star Microwave	8-11 GHz Microwave Circulator
AT1	MCL BW	Mini-Circuits	dc-18 GHz 3 dB attenuator
AT2	FP-50	Texscan	3 dB BNC attenuator
T1-2	MCL ANNE-50+	Mini-Circuits	dc-20 GHz 50 Ω termination, SMA(m)
DC1, DC2	E3648A	Agilent	100 W dual output DC power Supply
DC3	E3620A	Agilent	50 W dual output DC power Supply
DC4	E3649A	Agilent	100 W dual output DC power Supply
SP1	T1000	Anzac	10-1,000 MHz power splitter
SW1	MSN-10DT-05-DEC-MP	AMC	SP10T absorptive switch, 0.5 GHz-18 GHz
SW2-5	8762B TTL T24	Agilent	SP2D coaxial switch, dc-18 GHz
SW6	DSS-8+	D-Link	8 10/100 port LAN switch
GPIB1	82357B	Agilent	USB to GPIB interface
PCIE1	M9045B	Agilent	PCIe laptop card adapter Gen 1x4
PC1	HP Elitebook 8560P	Hewlett Packard	Laptop running Vee Pro 9.3, VSA 16.0, Signal Studio for Pulse Building

MIMO system is obtained. The data is stored in Matlab compatible .mat files.

3.3.2 Signal processing algorithms

The signal processing algorithms consist of pulse compression, array calibration, and MIMO beamforming.

De-chirping of the 64 received signals is performed by complex multiplication with the complex conjugate of the transmitted waveform. A fast Fourier transform then provides a pulse compressed range profile for each of the 64 channels.

Array calibration is performed by using the 64 range profiles and the known positions of the antenna array elements and of the calibration target located at 35 m range. For each transmit-receive element pair, the delay and phase due to propagation from the transmit element to the calibration target and back to the receive element are determined. The corresponding range profile is then shifted in range. This is a coarse correction for cable lengths and various delays introduced by the equipment. A finer correction is then applied as a phase correction. This process is repeated for all combinations of transmit and receive channels, producing 64 calibrated range profiles.

MIMO beamforming is performed using the following delay-and-sum method. The two-way distance and phase due to propagation from transmit antenna A to a given point in space and back to receive element B, is determined. The two-way distances and phases for all combinations of transmit and receive elements are determined. The two-way distances are used to pick the signals as a linear interpolation from the appropriate range bins in the calibrated range profiles. The phases are used to compensate the received signals. For beamforming using a MIMO-1 configuration, the resulting 64 phase compensated complex signals corresponding to the point in space are summed. For beamforming using any other MIMO configuration such as MIMO-2, the appropriate subset of the 64 phase compensated complex signals are summed. This process is repeated for all points in the space of interest. Typically, a grid in space is defined at the range of the targets (around 45 meters) and for angles varying between -40 and +40°. In Section 4, the results are plotted as an azimuth profile at the range of maximum intensity as a function of azimuth angle. The azimuth profile is displayed as relative power levels or as normalized power, in units of decibels. This azimuth profile indicates the beamforming capability of the considered array.

Given that the MIMO beamforming algorithm for this report is a simple sum of the appropriate signals and no scaling is applied, we expect different power levels between the MIMO configurations. Explicitly, the power level in decibels scales as

$$10 \log_{10}(N_{Tx} N_{Rx})^2, \tag{17}$$

where N_{Tx} and N_{Rx} are the number of transmit and receive elements, respectively. For MIMO-1, $N_{Tx} = N_{Rx} = 8$ and for MIMO-2, $N_{Tx} = 2$ while $N_{Rx} = 7$, leading to a 13 dB difference.

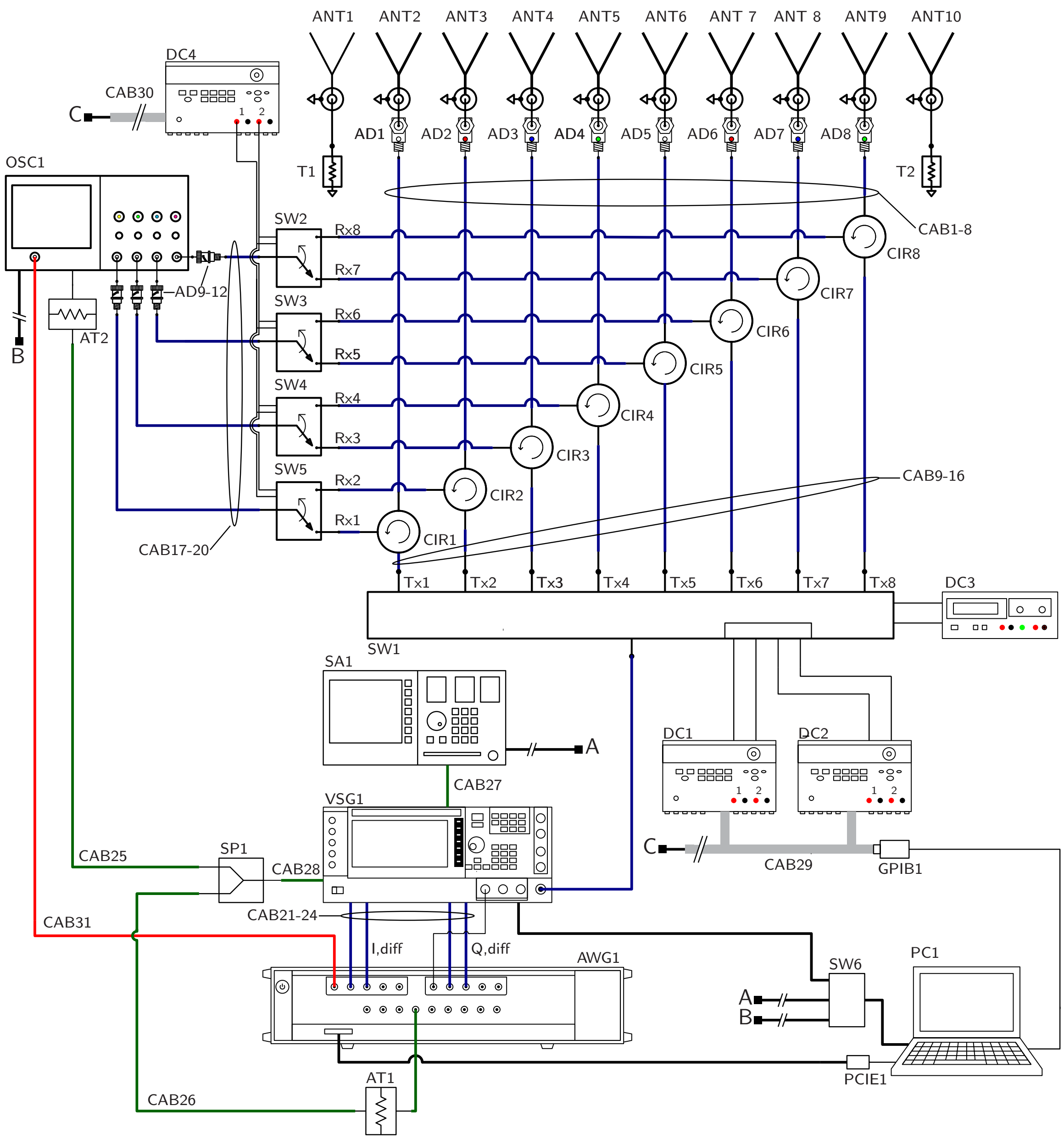

Figure 4: *Schematic of the equipment setup assembled for the time-division MIMO experiment.*

3.4 Mixed Experiments and Simulations Approach (MESA)

The purpose of MESA is to determine the frequency response, and hence the impulse response of the system composed of the 8 antennae and scene of observation including the targets. By determining this information, the data can be used with a system simulator to study the effects of changing system parameters such as Tx waveform characteristics and adding impairments such as nonlinear distortion and noise to the system. In this study, the 8-port S-parameters of the antenna array and observation scene were measured and the data was imported into Agilent ADS electronic design automation (EDA) software in order to simulate an ideal phased-array radar. The measurement and simulation procedure is described in the following sections.

3.4.1 Measurement Setup

The test setup used to measure the S-parameters is shown in Figure 5 and the equipment list is described in Table 3. The VNA is connected to the 12 port test set such that the full 8-port S-parameters of the antenna-array and scene can be measured. A two-port ECAL module along with an unknown THRU standard is used to perform the 8-port calibration [18]. The unknown THRU consists of a high quality phase stable microwave cable and two SMA adapters. One port of the E-CAL module is connected to each port of the test set and then the unknown THRU is successively connected between two ports of the test set. The VNA software minimizes the number of connections necessary between the ports in order to extract all the error terms required for the calibration.

The S-parameters were measured for run scene5, consisting of P1 and PC and run scene9, consisting of P4 and PC.

3.4.2 VNA Setup

In order to obtain a good impulse response, the VNA is setup to sweep over a wide band. The lower frequency is limited by the VNA at 10 MHz and the higher frequency is set to 18 GHz, which is the highest frequency for which the components in the setup are rated.

The frequency step size must be small enough such that the frequency response is not undersampled. The change in phase $\Delta\phi$ of the S-parameter per change in frequency Δf must be less than 180° based on the two-way time delay to the furthest target of interest, i.e.

$$\Delta\phi = 2\pi\Delta f\left(\frac{2R_{max}}{c}\right) \leq \pi \tag{18}$$

$$\text{or } \Delta f \leq \frac{c}{4R_{max}}, \tag{19}$$

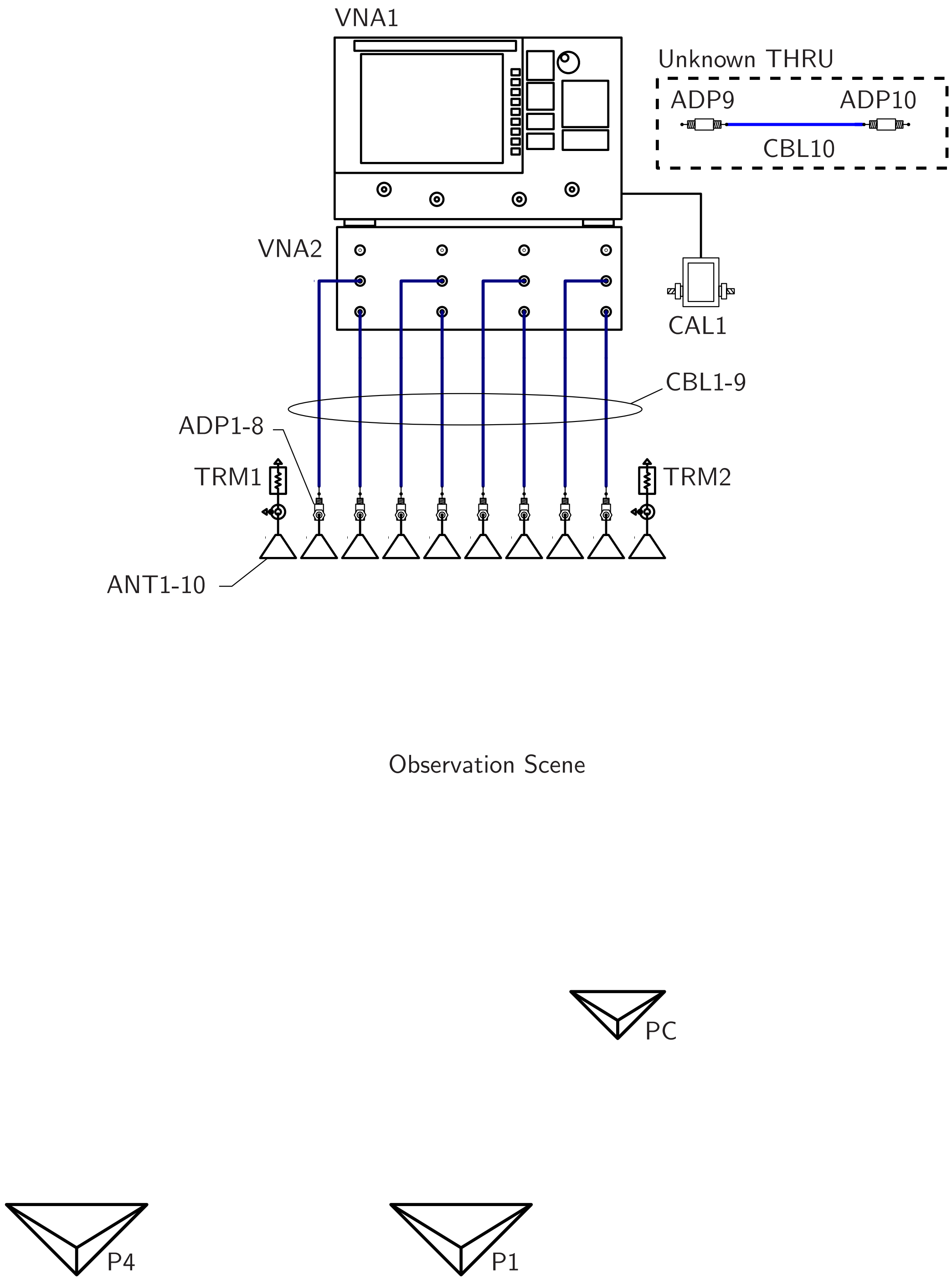

Figure 5: *Setup used to measure multi-port S-parameters*

Table 3: *Equipment used for S-parameter measurement.*

Designator	Part	Manufacturer	Description
ADP1-8	–	–	N-female to SMA-male adapter
ADP9-10	–	Southwest Microwave	SMA-female to SMA-female adapter
ANT1-10	640	Narda	8.2 - 12.4 GHz standard gain horn
CAL1	N4691-60006	Agilent	300 kHz - 26.5 GHz E-cal module
CBL1-9	Sucoflex 104PEA	Huber & Suhner	2.5 m RF cables N-male, SMA male
CBL10	Accu-Test 150	Teledyne Storm	18" RF cable
TRM1-2	ANNE-50X+	Mini-Circuits	50 Ω SMA-male termination
VNA1	N5242A	Agilent	4 port VNA
VNA2	U3042A E12	Agilent	12 port test set
P4	DREO	–	Trihedral corner reflector, $l = 75$ cm
P1	DREV	–	Trihedral corner reflector, $l = 75$ cm
PC	Athena	–	Trihedral corner reflector, $l = 69.6$ cm

where R_{max} is the maximum range of interest and c is the speed of light. Assuming $R_{max} = 50$ m, then it is found that the frequency step Δf must be less than 1.5 MHz. However, for the software to calculate a good impulse response it is suggested that there should be at least 6 samples per 360° phase change [19]. As a result, (19) is modified to:

$$\Delta f \leq \frac{c}{10R_{max}} \tag{20}$$

and $\Delta f \leq 600$ kHz.

Selection of the IF bandwidth, BW_{IF} involves a tradeoff between measurement speed and noise floor. Based on the PNA-X specifications [20], the typical noise floor of the test ports at X-band is -117 dBm in a 10 Hz bandwidth which translates to a noise density, N_d of -127 dBm/Hz. The noise floor of the measurement can be calculated from:

$$N_{floor} = N_d BW_{IF}. \tag{21}$$

An estimate of the received signal strength can be made using the radar range equation and the ideal radar cross section for a trihedral corner reflector. For a trihedral corner reflector with sidelength l, at wavelength λ the radar cross section, σ_{tgt} is given by [21]:

$$\sigma_{tgt} = \frac{4\pi l^4}{3\lambda^2}. \tag{22}$$

The received signal-to-noise ratio is given by:

$$SNR = \frac{P_T G_{ant}^2 \lambda^2}{(4\pi)^3 R^4 N_{floor}} \sigma_{tgt} \tag{23}$$

where G_{ant} is the gain of the antenna, R is the range, and P_T is the transmit power.

Substituting (21) and (22) into (23) results in

$$SNR = \frac{P_T}{3N_d BW_{IF}} \left(\frac{G_{ant}}{4\pi}\right)^2 \left(\frac{l}{R}\right)^4. \tag{24}$$

Assuming the following:

P_T	is the transmit power, 8 dBm. This is the maximum power that could be transmitted without overloading the instrument.
N_d	is the noise density of the VNA input ports, -127 dBm/Hz typical at X-band.
BW_{IF}	is the bandwidth of the VNA IF receiver. This parameter is adjustable and was set to 1 kHz.
R	is the range to the farthest target, 45 m.
l	is the side length of the corner reflector, 75 cm.
G_{ant}	is the gain of the antenna, 15.4 dBi.

The SNR is approximately 38 dB which was more than adequate for this measurement. A summary of all the VNA settings for the measurement is given in Table 4.

Table 4: *VNA Parameters used for measurement and calibration.*

Parameter	**Value**	**Units**
Start Frequency	10	MHz
Stop Frequency	18.01	GHz
Step Frequency	562.5	kHz
No. of points	32001	—
IF Bandwidth	1	kHz
Transmit Power	8	dBm

3.4.3 Simulation

The measured 8-port S-parameters for the observation scene were imported into Agilent ADS in order to simulate an ideal phased-array radar. The first step was to calibrate the array to account for differences between the antenna ports due to cable lengths, adaptors, etc. This was done by performing a transient simulation. Each port of the array was independently stimulated with an linear frequency-modulated (LFM) signal at a center frequency of 9 GHz and bandwidth of 2 GHz. The monostatic returns from each port were multiplied by the replica of the transmit signal and the resulting signal was transformed to the frequency domain. The returns from each target appear at frequencies proportional to their range and the chirp rate. A result is shown in Figure 6(a) for an uncalibrated array. The appropriate delays were added to each port of the array until all the peaks were aligned and the phase differences between the ports were minimized. This result is shown in Figure 6(b).

The phased-array simulations were carried out using an LFM source at a center frequency of 9 GHz with a bandwidth of 150 MHz, the same parameters as were used for the MIMO measurements, as described in Section 3.3. The array was steered over the observation scene at a determined angle and the returns were pulse compressed and then power combined to obtained the final output. For example using the data from run scene9, when the array is steered to 14.8° such that it is pointing directly at P4, we obtain the output power as a function of range shown in Figure 7. The returns from P4, PC and also those due to antenna return loss are clearly visible.

For each data set, the array was steered to angles ±15° around the target of interest, and the resulting target output power was determined as a function of angle.

Alternatively, the measured 8-port S-parameters were processed as a MIMO array. The same LFM source was used in the Agilent ADS simulations but the array was not steered and the channels were not power combined. The pulse compressed range profiles were processed as described in Section 3.3.2.

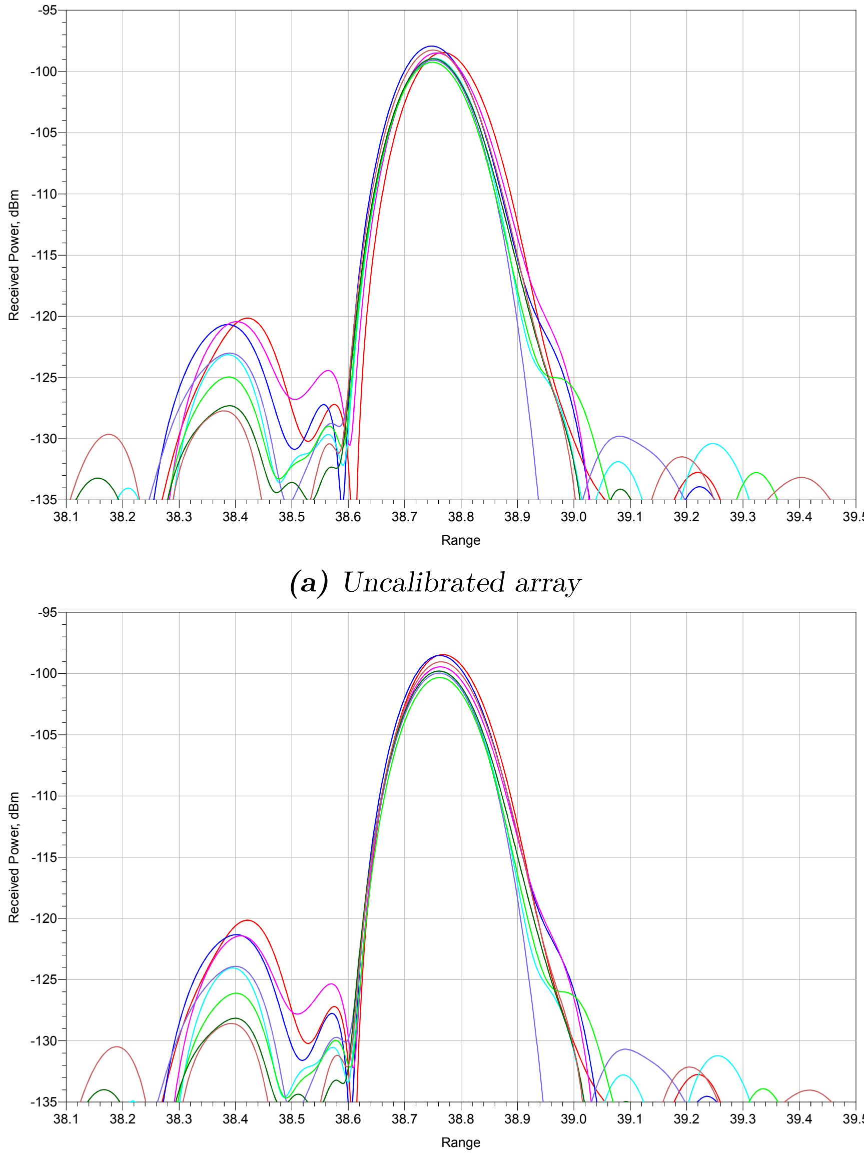

(a) *Uncalibrated array*

(b) *Calibrated array*

Figure 6: *Returns from calibration target PC. The 8 colours correspond to the 8 receive channels.*

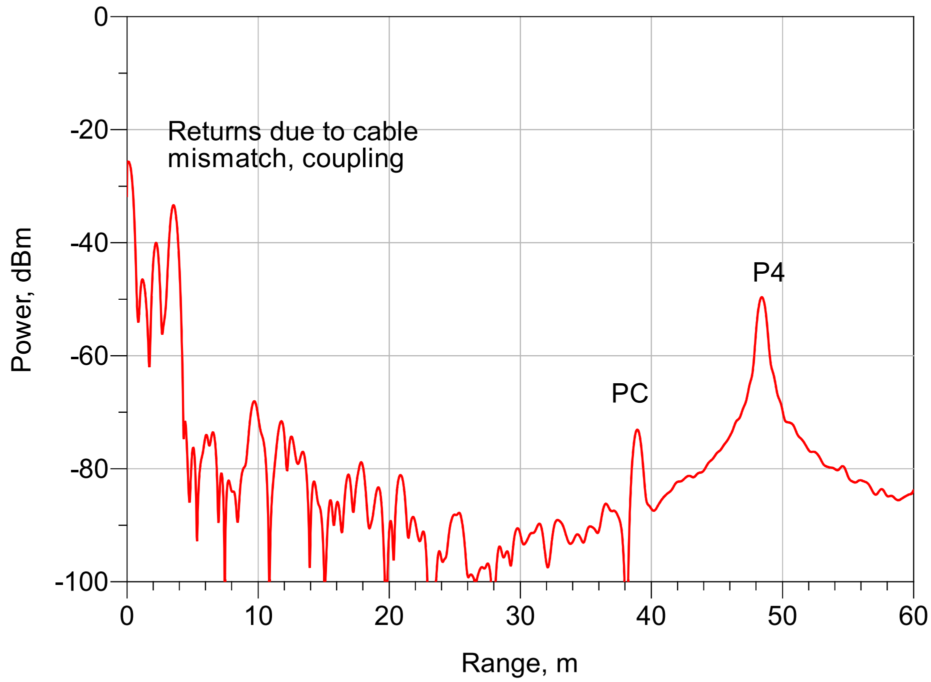

Figure 7: *Received signal from phased array simulation for scene 9 at azimuth angle = 14.8° The antenna array is electrically steered toward target P4.*

4 Experimental results

In this Section are presented the experimental results obtained with the MIMO array. The results obtained with the time-division 8-channel radar, processed with a MIMO-1 configuration, are presented in Section 4.1. The MESA data, collected using the VNA and processed in simulations using the ADS software, are presented in Section 4.2 to demonstrate that the MIMO-1 and phased array factors are identical. Finally, a comparison between the MIMO-1 and MIMO-2 configurations is provided in Section 4.3 using the time-division 8-channel radar data.

4.1 MIMO-1 array (8 transmit elements and 8 receive elements)

In this section are grouped the results obtained by processing the time-division radar data using a MIMO-1 configuration with 8 transmit and 8 receive elements.

4.1.1 One target scenes

In Figures 8 to 12 are shown the experimental data beamformed with a MIMO-1 configuration for the scenes with one target. The MIMO beamforming algorithms were described in Section 3.3.2. The theoretical array factors for the 2-way radiation pattern are shown for comparison, ignoring the element factor. The theoretical array factors are scaled in amplitude to match the experimental data and steered in azimuth toward the target location at θ_0, according to:

$$A_N(\theta) \;=\; \frac{\sin^2[N\pi(d/\lambda)(\sin\theta - \sin\theta_0)]}{N^2\,\sin^2[\pi(d/\lambda)(\sin\theta - \sin\theta_0)]}. \tag{25}$$

For each of these graphs, we see that the main beam matches the ground truth of the target location. We observe the grating lobes, as expected. The experimental data matches the theoretical antenna pattern especially for the main lobe and the first sidelobe. Scene 2 (Figure 11) matches particularly well the theoretical antenna pattern, even for the sidelobes.

The experimental data for the same five scenes are overlaid on the graph of Figure 13, to illustrate the difference in power levels. The Figure shows the azimuth profiles after beamforming, but the range compressed responses exhibit the same power level variations from scene to scene (graph not shown). These power level variations cannot be explained by the element factor of the antenna element, which has a beamwidth of approximately 32° in the azimuth direction [17]. The element factor accounts for only a 6 dB decrease between the target at boresight and the one located at +14.8°. Even scenes 2 and 3, with the target located at the same position in azimuth, show a 7 dB difference in the main beam power level. In Annex A, it is demonstrated

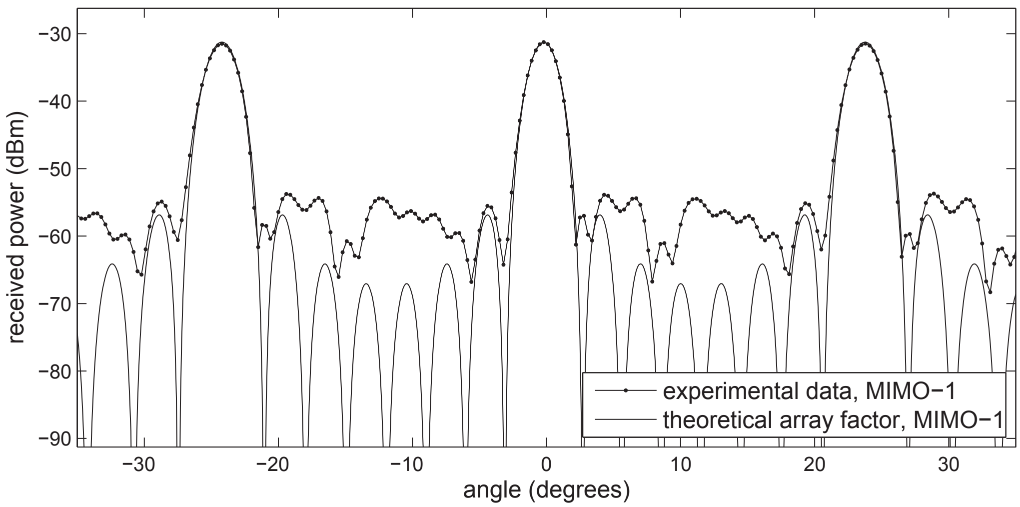

Figure 8: *Azimuth profile for scene 5 with one target located at -0.4°. The theoretical array factor, scaled and steered in azimuth, is shown for comparison.*

that ground multipath can most likely explain the different power levels, especially for scenes 2 and 3 with the target at the same azimuth location but different heights above the ground.

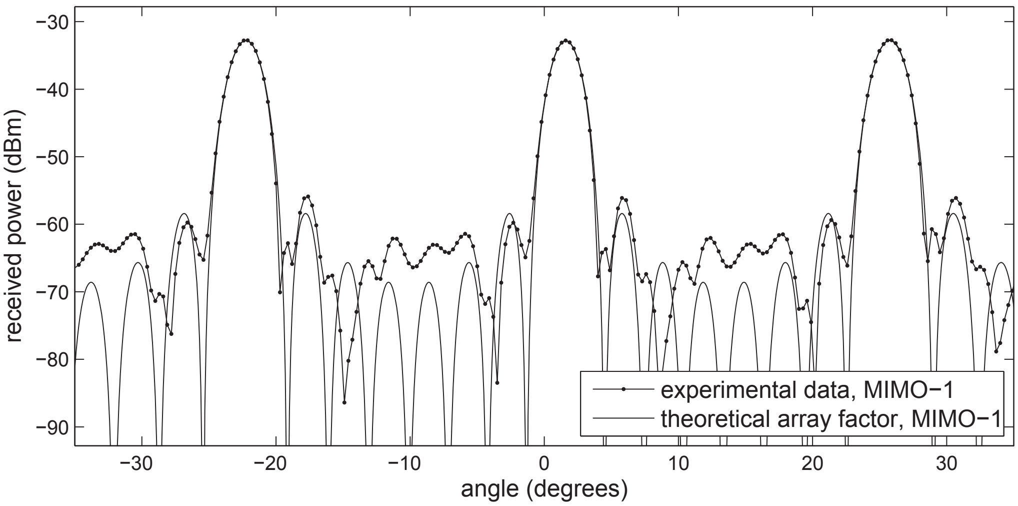

Figure 9: *Azimuth profile for scene 7 with one target located at +1.6°. The theoretical array factor, scaled and steered in azimuth, is shown for comparison.*

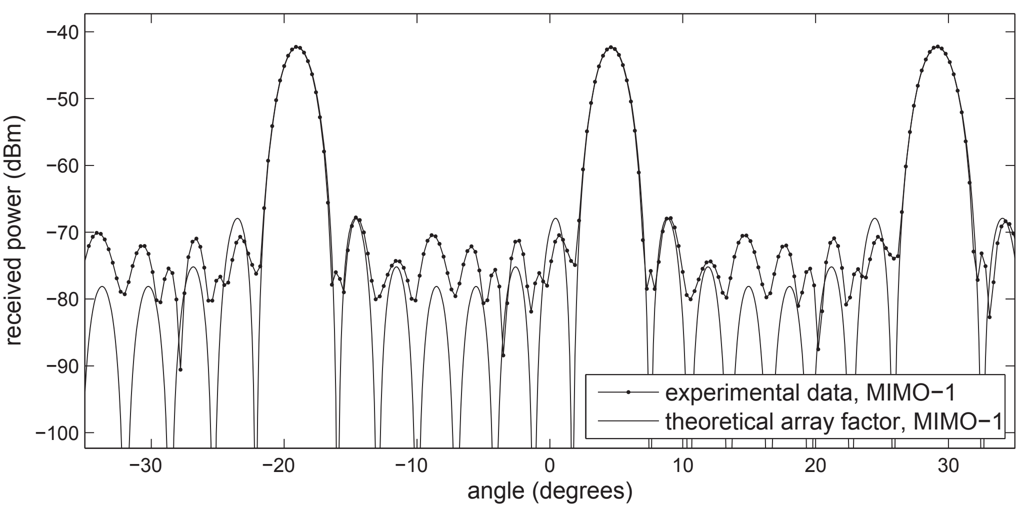

Figure 10: *Azimuth profile for scene 3 with one target located at +4.6°. The theoretical array factor, scaled and steered in azimuth, is shown for comparison.*

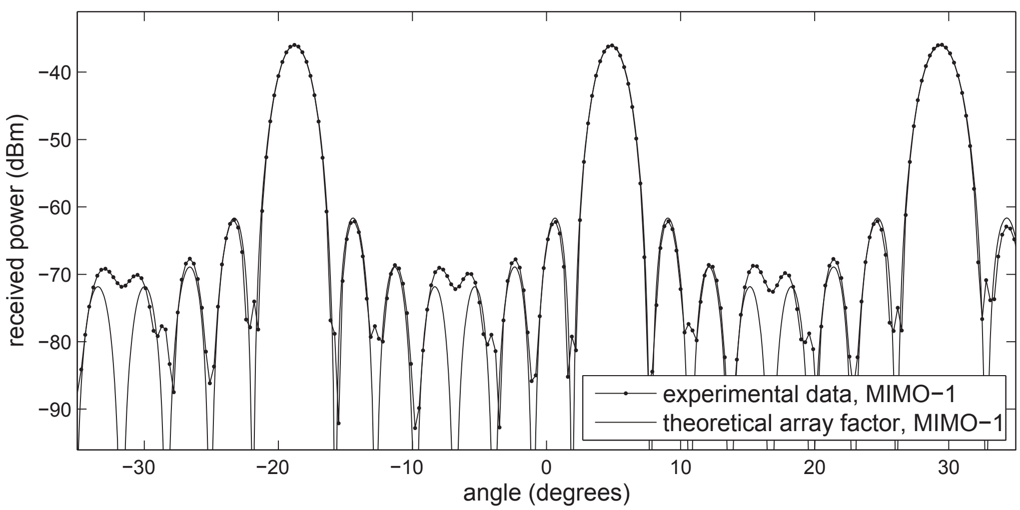

Figure 11: *Azimuth profile for scene 2 with one target located at +4.6°, lower height. The theoretical array factor, scaled and steered in azimuth, is shown for comparison.*

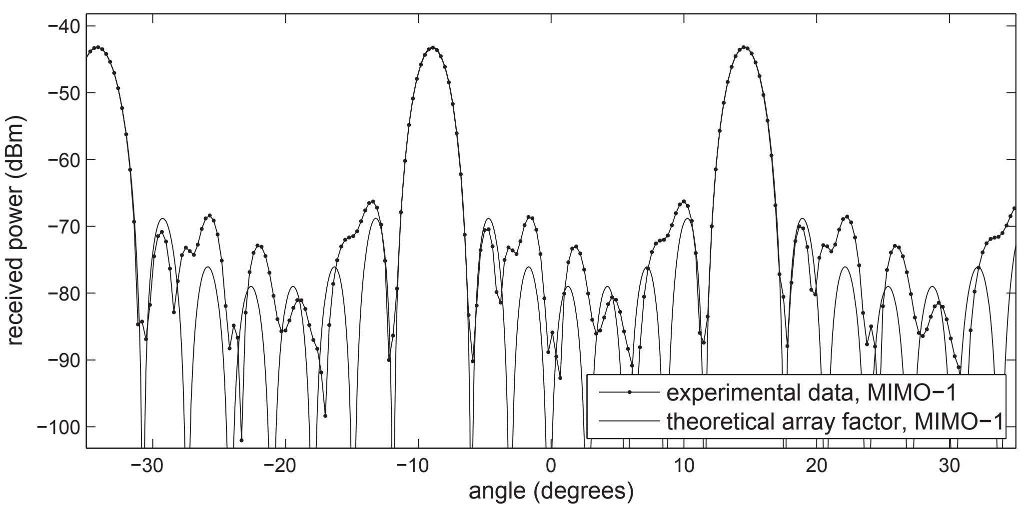

Figure 12: *Azimuth profile for scene 9 with one target located at +14.8°. The theoretical array factor, scaled and steered in azimuth, is shown for comparison.*

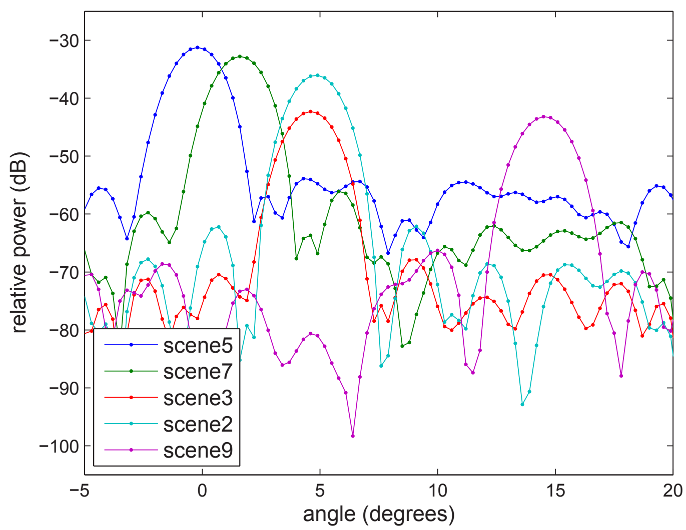

Figure 13: *Azimuth profile for scenes 5, 7, 3, 2, and 9 with one target at various locations in azimuth.*

4.1.2 Two target scenes

In Figures 14 to 16 are shown the time-division radar data for the scenes with two targets. For each graph, the experimental data of the corresponding scenes with one target only are displayed for comparison.

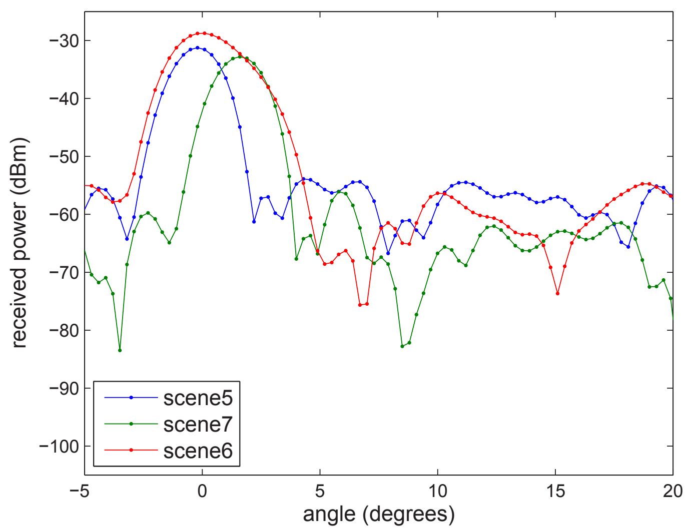

Figure 14: *Azimuth profile for scene 6 with two targets located at -0.4° and +1.6°. The azimuth profiles for scene 5 (one target at -0.4°) and scene 7 (one target at +1.6°) are displayed for comparison.*

For scene 6 with two targets located 2.1° apart (Figure 14), the resolution of the MIMO-1 array is not sufficient to discriminate between the two targets.

For scene 4 with two targets located 5° apart (Figure 15), the two targets are resolved, but we notice that the target at +4.6° (scene 4, red curve) appears with a relative power 1.3 dB lower than it appears when it is the only target in the scene (scene 2, green curve). On the other hand, the target at -0.4° (scene 4, red curve) appears with a relative power 1.5 dB higher than it appears when it is the only target in the scene (scene 5, blue curve). The target at +4.6° was not moved between the scene3 and scene4 data acquisitions, and the target at -0.4° was not moved between the scene4 and scene5 data acquisitions. It is hypothesized that there is interaction between the two trihedrals on the field.

For scene 8 with two targets located 13.2° apart (Figure 16), the two targets are resolved. The two trihedrals are far enough to not interact, and the experimental data for two targets coincide with the experimental data for each target individually, as expected.

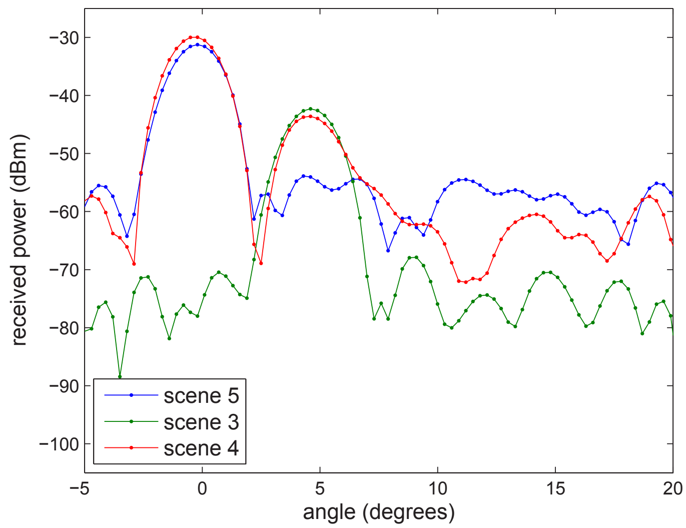

Figure 15: *Azimuth profile for scene 4 with two targets located at -0.4° and +4.6°. The azimuth profiles for scene 5 (one target at -0.4°) and scene 3 (one target at +4.6°) are displayed for comparison.*

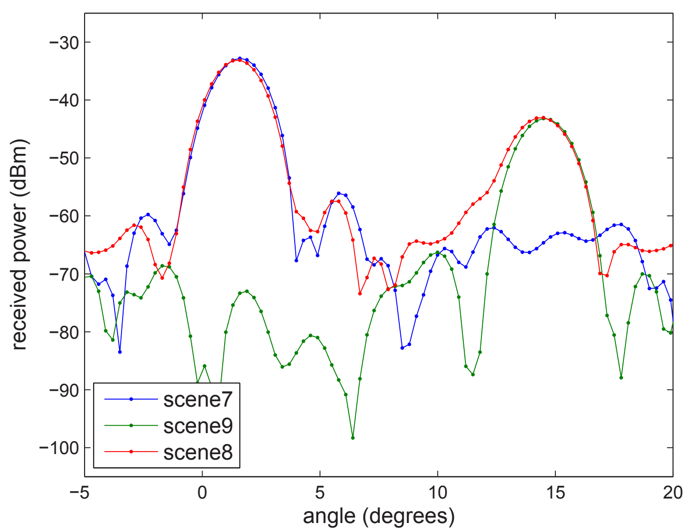

Figure 16: *Azimuth profile for scene 8 with two targets located at +1.6° and +14.8°. The azimuth profiles for scene 7 (one target at +1.6°) and scene 9 (one target at +14.8°) are displayed for comparison.*

4.2 Phased array results obtained with MESA (8 transmit elements and 8 receive elements)

In this section, it is demonstrated experimentally that the phased array 2-way antenna pattern and the MIMO-1 configuration have identical array factors. In Figures 17 and 18 are shown the results for scenes 9 and 5, respectively. Each graph shows four curves. The theoretical two-way array factor is shown as a solid line. The time-division radar data processed with a MIMO-1 configuration are shown as dots. The MESA data processed as a phased array simulation, as described in Section 3.4, are shown as circles. Finally, the MESA data processed as a MIMO-1 configuration are shown as triangles. All curves are shown on a normalized scale since the time-division radar data and the MESA data have different received power levels due the different setup and cables.

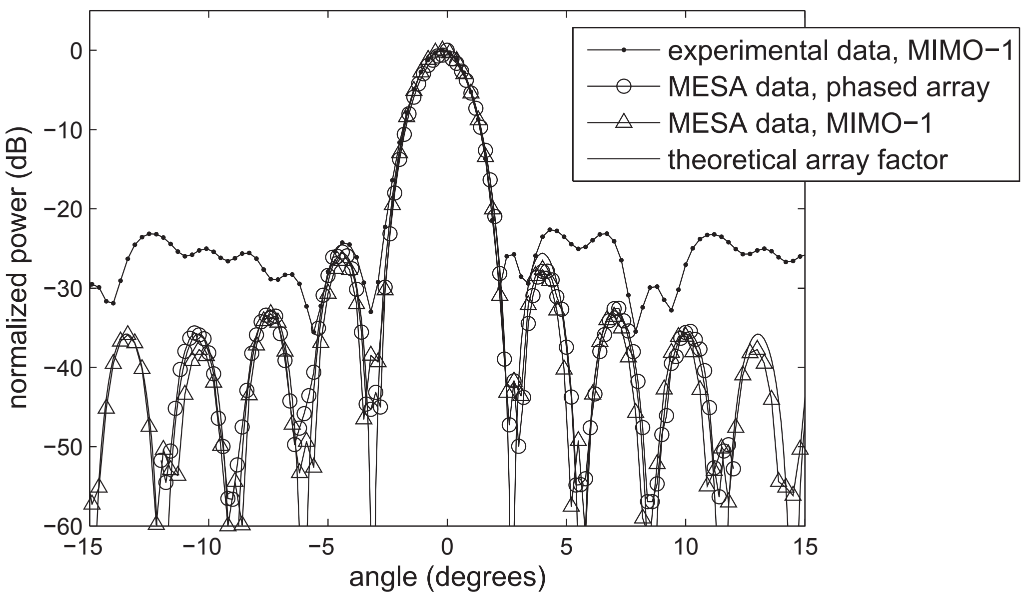

Figure 17: *Azimuth profile for scene 5 with one target located at -0.4°, for the time-division MIMO-1 radar data, the MESA data processed as phased array and as MIMO-1. The theoretical array factor, steered in azimuth, is shown for comparison.*

The four curves are in agreement in terms of the main beam location and width. We see a discrepancy in the sidelobes. The MESA data, either processed as MIMO-1 or phased array, show lower sidelobe levels than the time-division radar data. The fact that the MESA data shows similar sidelobe levels for both MIMO-1 and phased array simulations indicates that the higher sidelobes of the time-division data are not due to the MIMO processor. Rather, the time-division data were acquired as 8-bit data and suffer from lower dynamic range. Furthermore, they were acquired with multiple

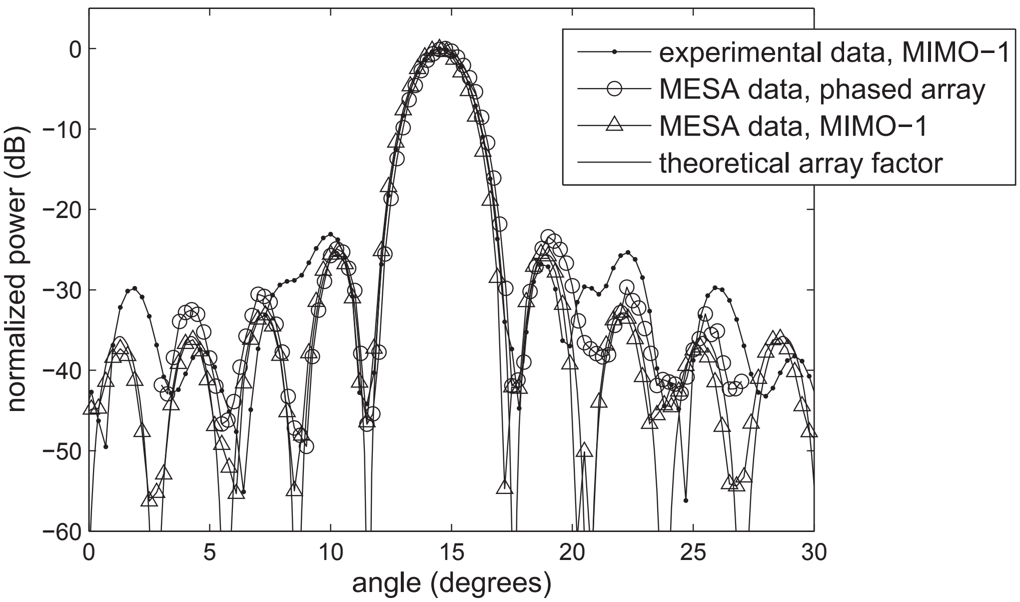

Figure 18: *Azimuth profile for scene 9 with one target located at +14.8°, for the time-division MIMO-1 radar data, the MESA data processed as phased array and as MIMO-1. The theoretical array factor, steered in azimuth, is shown for comparison.*

triggers which can cause jitter issues. We believe that these effects are small enough to not affect the study of the MIMO angle accuracy, but are large enough to affect the sidelobe structure levels.

4.3 Comparison of MIMO-1 and MIMO-2 arrays

In this section are compared the azimuth profiles of the time-division radar data processed using both MIMO-1 and MIMO-2 arrays.

4.3.1 One target scene

In Figure 19 is shown the time-division radar data for scene 2 with one target at $+4.6^{\circ}$ and lower height, processed for both MIMO-1 and MIMO-2 arrays. On the top graph, the azimuth profiles are shown as normalized values. We can clearly see the improved resolution of the MIMO-2 array over the MIMO-1 array, at the expense of larger sidelobes (13 dB versus 26 dB main-to-first sidelobe ratio for the MIMO-2 and MIMO-1 arrays, respectively). On the bottom graph, the azimuth profiles are shown without normalization and we see the gain loss of approximately 13 dB for MIMO-2 array, as expected since only two transmit elements are used instead of all 8 elements for the MIMO-1 array.

4.3.2 Two target scenes

In Figures 20 to 22 are shown the azimuth profiles for the scenes with two targets, processed for both MIMO-1 and MIMO-2 arrays. We see the effect of slightly increased resolution for all cases, at the expense of larger sidelobes for MIMO-2. Given the issues of ground multipath and interaction between targets discussed above, the resulting signatures for the two targets can result in power values differing by as much as 13 dB. Using a MIMO-2 array, the weaker target now appears at approximately the same power level as the sidelobes of the stronger target. As a result, the signature of the weaker target appears as the constructive or destructive sum of the target signal itself and the stronger target sidelobes. In particular, the weaker target of scene 8 appears 10 dB lower than the stronger target for MIMO-1, while it appears 14 dB lower for MIMO-2 (Figure 22).

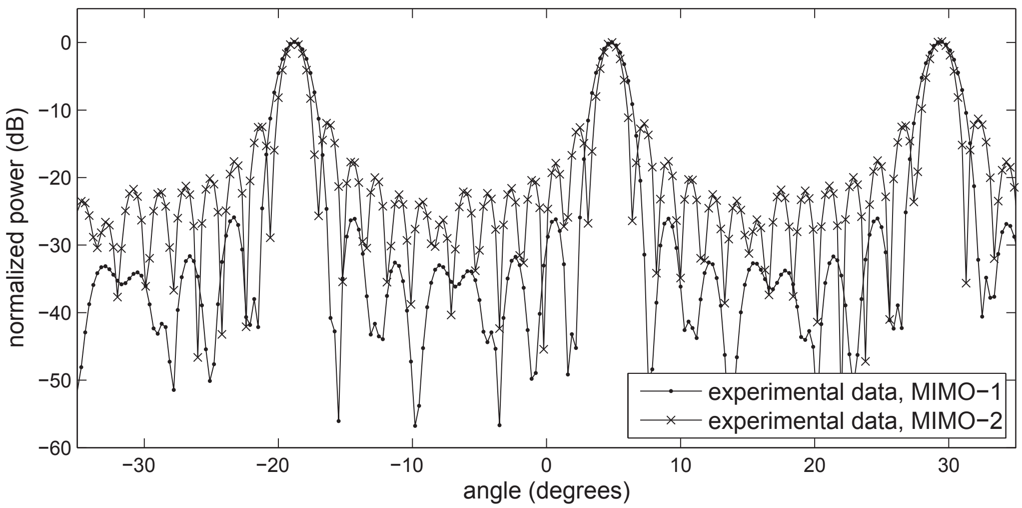

(a) *Normalized power values*

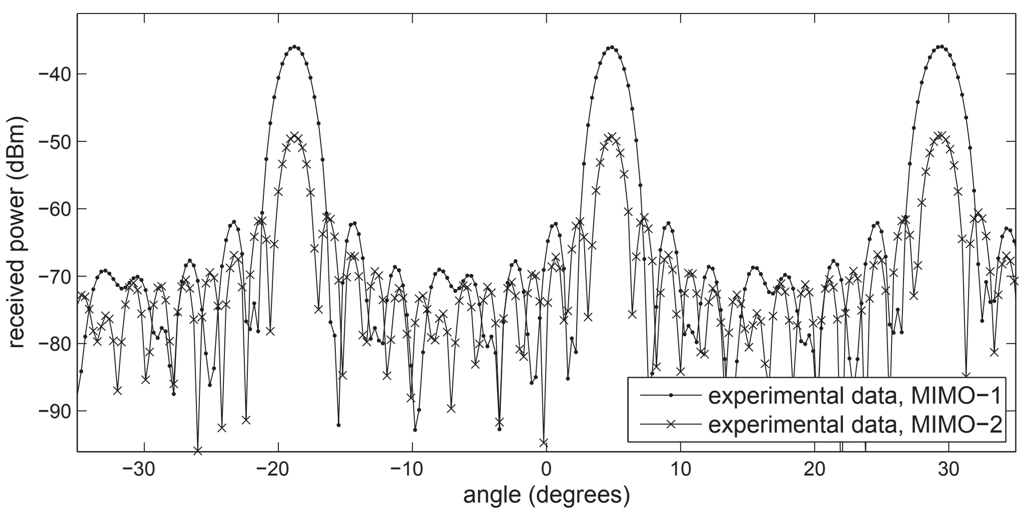

(b) *Received power values*

Figure 19: *Azimuth profiles for scene 2 with one target located at +4.6°, lower height, processed for both MIMO-1 and MIMO-2 arrays.*

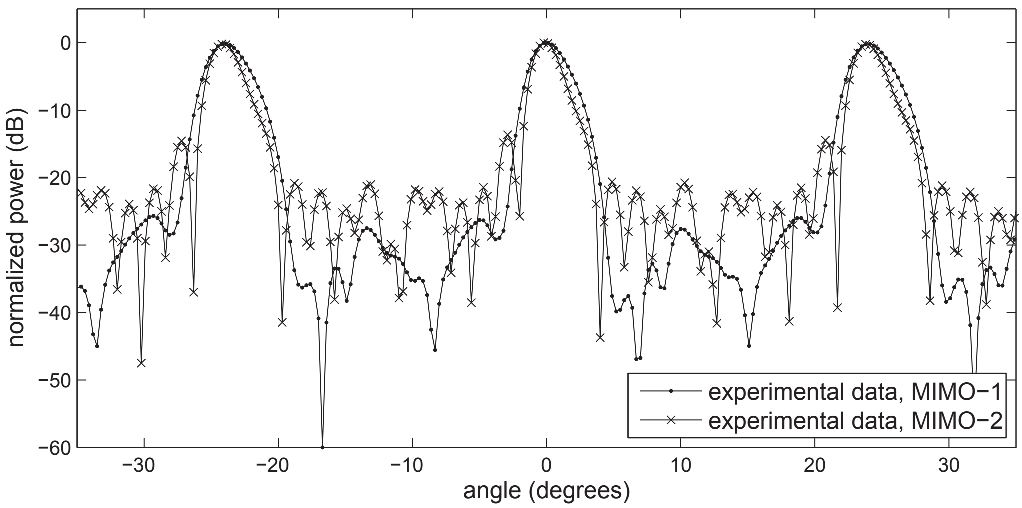

(a) *Normalized power values*

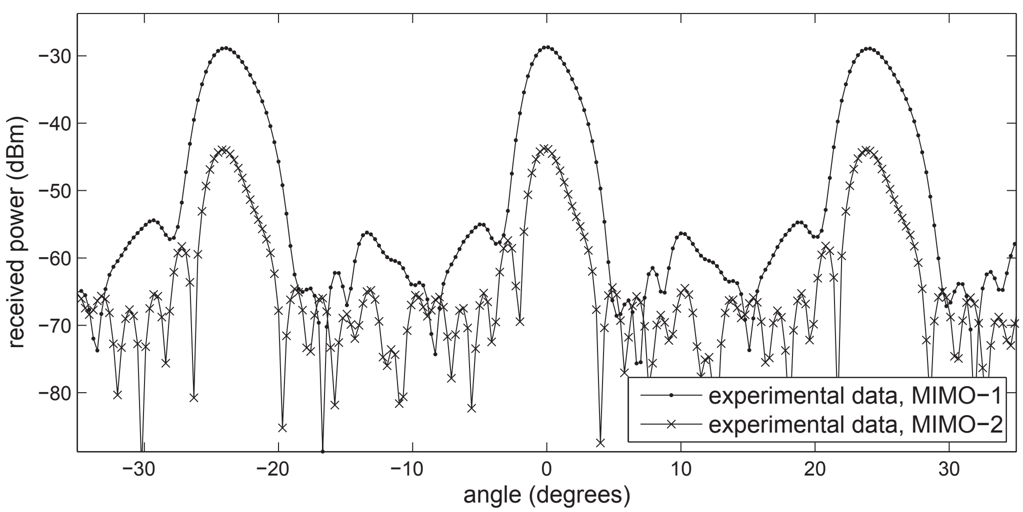

(b) *Received power values*

Figure 20: *Azimuth profile for scene 6 with two targets located at -0.4° and +1.6°, processed for both MIMO-1 and MIMO-2 arrays.*

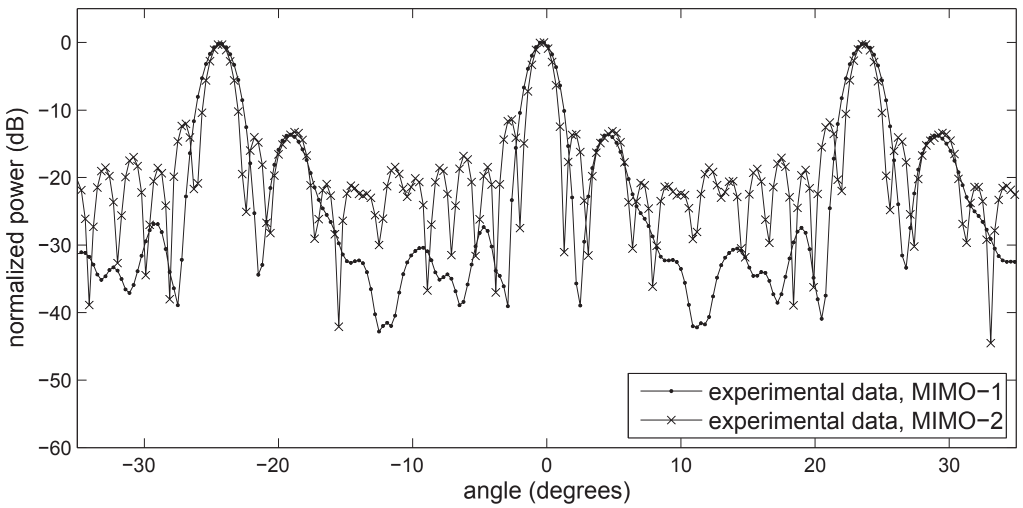

(a) *Normalized power values*

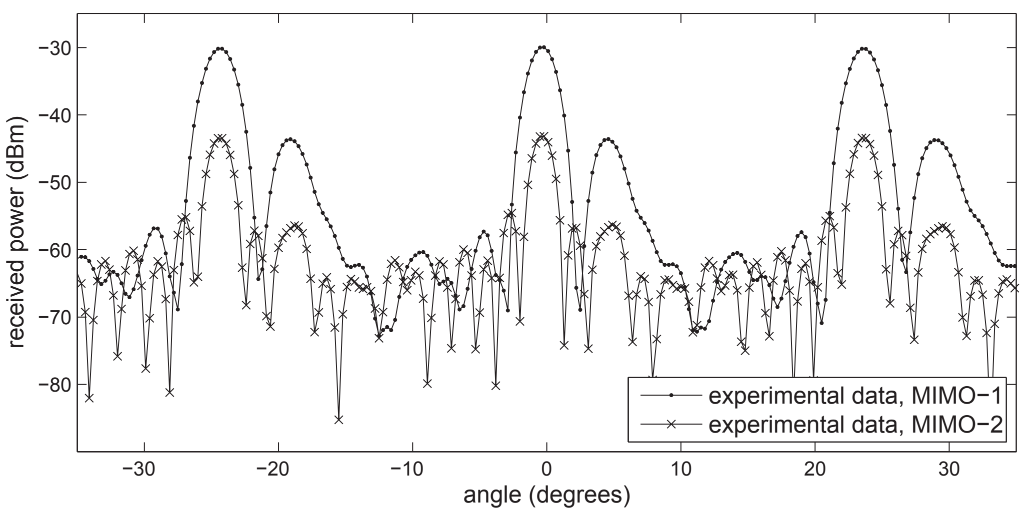

(b) *Received power values*

Figure 21: *Azimuth profile for scene 4 with two targets located at -0.4° and +4.6°, processed for both MIMO-1 and MIMO-2 arrays.*

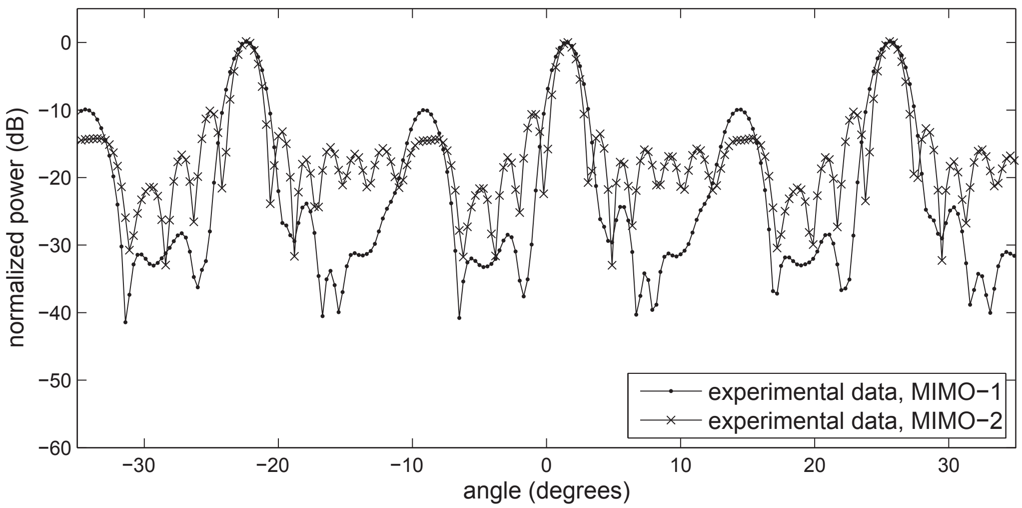

(a) *Normalized power values*

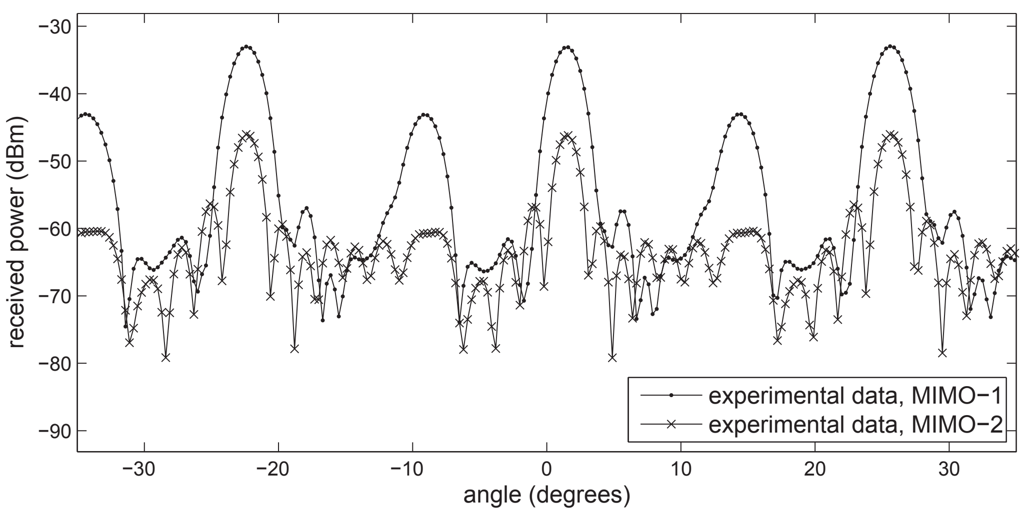

(b) *Received power values*

Figure 22: *Azimuth profile for scene 8 with two targets located at +1.6° and +14.8°, processed for both MIMO-1 and MIMO-2 arrays.*

5 Discussion and conclusions

In this report, we have demonstrated experimentally that the MIMO-1 array factor is equal to the 2-way phased array factor, as predicted with the mathematical formulation of Section 2, for uniform phase and magnitude illumination.

We have further studied the MIMO-2 array configuration, for which we used two transmitters and seven receivers. We have demonstrated that the MIMO-2 configuration provides improved resolution and much reduced complexity, at the expense of gain loss and higher sidelobes. The reduced gain can be offset by the MIMO advantage of providing greater coverage and longer dwell times by illuminating the whole scene at once with orthogonal waveforms. This discussion is beyond the scope of this report.

The higher sidelobes of MIMO-2 array can be circumvented by using appropriate weighting of the MIMO channels before summation. Indeed, the MIMO-1 configuration can be viewed as a triangle weighting of the MIMO-2 configuration. The convolution of the transmit and receive arrays, i.e. the virtual array, is the convolution of two rectangle functions for the MIMO-1 configuration and results in a triangle with coefficients $[1, 2, 3, 4, 5, 6, 7, 8, 7, 6, 5, 4, 3, 2, 1]/8$ in our case. The virtual array of the MIMO-2 configuration is an array of 14 elements each with a coefficient of 1. In Figure 23, we have reproduced the results of Figure 19 for scene 2 for the MIMO-1 and MIMO-2 arrays. We also have plotted the results for MIMO-2 array using a triangle weighting with coefficients $[1, 2, 3, 4, 5, 6, 7, 7, 6, 5, 4, 3, 2, 1]/8$ to mimic as closely as possible the MIMO-1 array. The results show that using this weighting we can recover the results of MIMO-1 in terms of beamwidth and sidelobes, with much reduced complexity, at the expense of further gain loss.

As discussed in Annex A, an important limitation of this experiment is the presence of ground multipath. It has limited our capability to demonstrate the benefits of increased resolution with the MIMO-2 array, given that the two targets in a scene appeared with different power levels as a result of multipath with different heights above the ground. In a future experiment, this effect could be minimized by a careful choice of heights, and by performing the experiments over grass rather than snow to minimize specular reflection.

Another limitation of this experiment is the time requirement to collect one data set. Given that we used time division, one data set required switching the transmit-receive channels 64 times. A future prototype could make use of waveforms with orthogonality based on different bands or coded waveforms, which would require an 8-channel receiver.

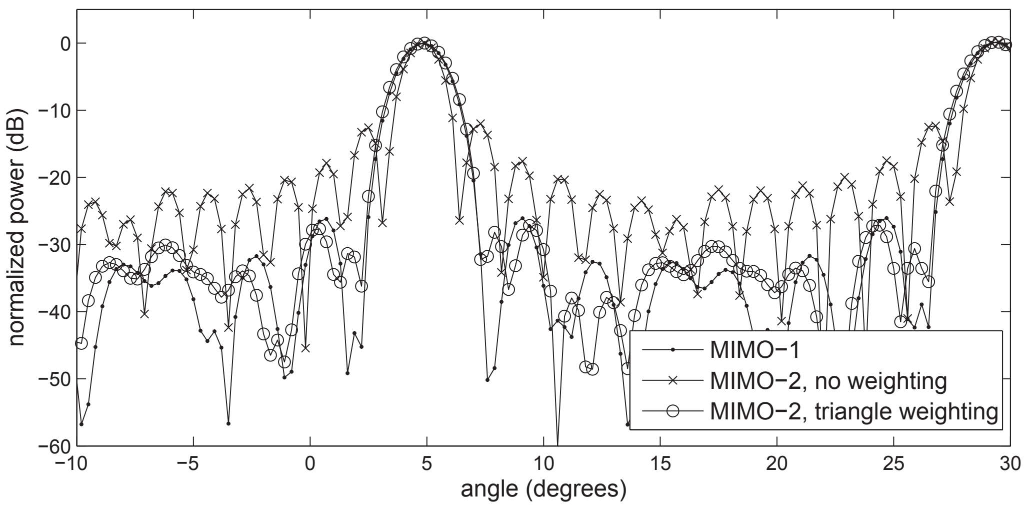

(a) *Normalized power values*

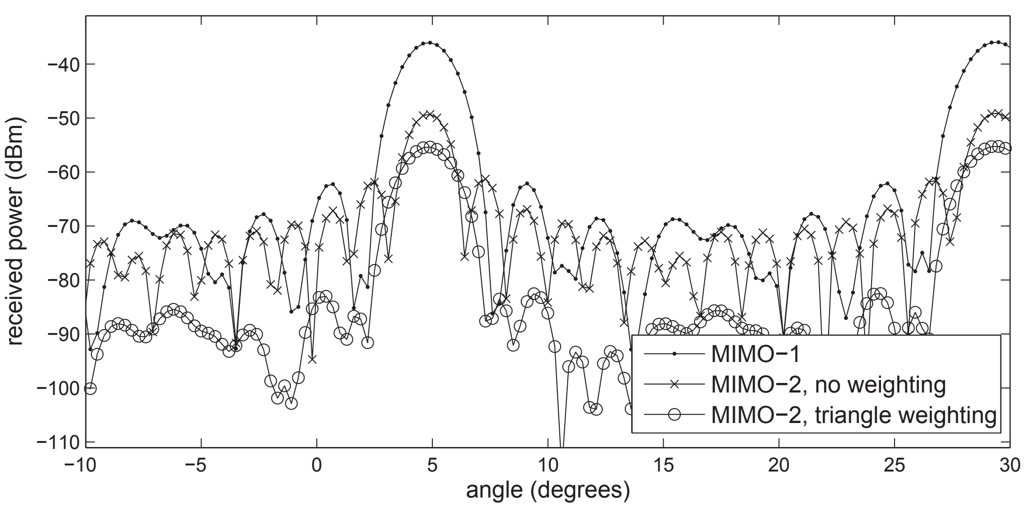

(b) *Received power values*

Figure 23: *Azimuth profiles for scene 2 with one target located at +4.6°, lower height, processed for MIMO-1, MIMO-2 with and without triangle weighting.*

This page intentionally left blank.

References

[1] Melvin, W. and Scheer, J. (2012), Principles of Modern Radar: Advanced Techniques, SciTech Publishing.

[2] Gini, F., Maio, A. D., and Patton, L. (2011), Waveform Design and Diversity for Advanced Radar Systems, The Institution of Engineering and Technology.

[3] Li, J. and Stoica, P. (2009), MIMO Radar Signal Processing, Wiley.

[4] Gesbert, D., Shafi, M., shan Shiu, D., Smith, P., and Naguib, A. (2003), From theory to practice: an overview of MIMO space-time coded wireless systems, *Selected Areas in Communications, IEEE Journal on*, 21(3), 281–302.

[5] Sévigny, P. (2009), Multiple-input multiple output (MIMO) radar: Literature survey of papers published between 2003 and September 2008, (DRDC Ottawa TM 2008-333) DRDC Ottawa.

[6] Stankovic, L. (2013), MIMO radar: Literature survey of papers published between September 2008 and December 2012, (DRDC Ottawa CR 2013-018) DRDC – Ottawa Research Centre.

[7] Stoica, P., Li, J., and Xie, Y. (2007), On Probing Signal Design For MIMO Radar, *IEEE Trans. Signal Processing*, 55(8), 4151–4161.

[8] Rabideau, D. (2009), Non-adaptive multiple-input, multiple-output radar techniques for reducing clutter, *Radar, Sonar Navigation, IET*, 3(4), 304 –313.

[9] Forsythe, K., Bliss, D., and Fawcett, G. (2004), Multiple-input multiple-output (MIMO) radar: performance issues, In *Conference Record of the Thirty-Eighth Asilomar Conference on Signals, Systems and Computers*, Vol. 1, pp. 310–315.

[10] Rabideau, D. and Parker, P. (2003), Ubiquitous MIMO multifunction digital array radar, In *Conference Record of the Thirty-Seventh Asilomar Conference on Signals, Systems and Computers*, Vol. 1, pp. 1057–1064.

[11] Bekkerman, I. and Tabrikian, J. (2006), Target Detection and Localization Using MIMO Radars and Sonars, *IEEE Trans. Signal Processing*, 54(10), 3873–3883.

[12] Robey, F., Coutts, S., Weikle, D., McHarg, J., and Cuomo, K. (2004), MIMO radar theory and experimental results, In *Conference Record of the Thirty-Eighth Asilomar Conference on Signals, Systems and Computers*, Vol. 1, pp. 300–304.

[13] Bliss, D. and Forsythe, K. (2003), Multiple-input multiple-output (MIMO) radar and imaging: degrees of freedom and resolution, In *Conference Record of the Thirty-Seventh Asilomar Conference on Signals, Systems and Computers*, Vol. 1, pp. 54–59.

[14] Forsythe, K. and Bliss, D. (2005), Waveform Correlation and Optimization Issues for MIMO Radar, In *Conference Record of the Thirty-Ninth Asilomar Conference on Signals, Systems and Computers*, pp. 1306–1310.

[15] Eaves, J. and Reedy, E. (1987), Principles of Modern Radar, Chapman and Hall.

[16] (2012), Leica TS15 User Manual, 3.1 ed, Leica Geosystems.

[17] English, E. K. (1980), Measuring Techniques for the Calibration of Standard Gain Horn Antennas, (Technical Report) DTIC Document.

[18] PNA Help Manual, A10.20 ed, Keysight Technologies.

[19] ADS: Transient/Convolution Questions on Using Frequency Domain Data (online), http://edadocs.software.keysight.com/display/eesofkcads/Transient+{\}and+convolution+questions+on+using+frequency+domain+data.

[20] (2014), Keysight 2-Port and 4-Port PNA-X Network Analyzer, Data Sheet and Technical Specifications, Keysight Technologies.

[21] Richards, M. A., Scheer, J. A., and Holm, W. A., (Eds.) (2010), Principles of Modern Radar, SciTech Publishing.

[22] Skolnik, M., (Ed.) (1990), Radar Handbook: second edition, McGraw-Hill.

[23] Mahafza, B. R. (2013), Radar systems analysis and design using MATLAB, Chapman & Hall.

[24] Hallikainen, M., Ulaby, F., and Abdelrazik, M. (1986), Dielectric properties of snow in the 3 to 37 GHz range, *Antennas and Propagation, IEEE Transactions on*, 34(11), 1329–1340.

Annex A Ground multipath

In this annex, we demonstrate using a flat-earth model that ground multipath is a likely cause of the power level fluctuations observed in the experimental MIMO data presented in this report.

As discussed in Section 3.1, the MIMO experiments were conducted outside on a relatively flat terrain covered by a thin layer of snow. The terrain was flat but could have a small slope. This terrain can be considered a good specular reflector. The height of the targets is known, relative to an arbitrary reference height, but the absolute height relative to the local ground is not known precisely. The radar height is estimated to be between 2.3 and 2.45 m relative to the average terrain height. Vertical polarization was used.

We use a flat-earth model as depicted in Figure A.1. The relative height of the different targets, as measured with the Leica TS15 Total Station, are tabulated in Table A.1. The targets were located at a range r_g of 45 m from the radar. As a result, the grazing angle Ψ at the point of reflection on the ground was approximately 6°. Both reflected and direct path rays are within the main beam of the antenna, thus there is no antenna pattern effect in elevation.

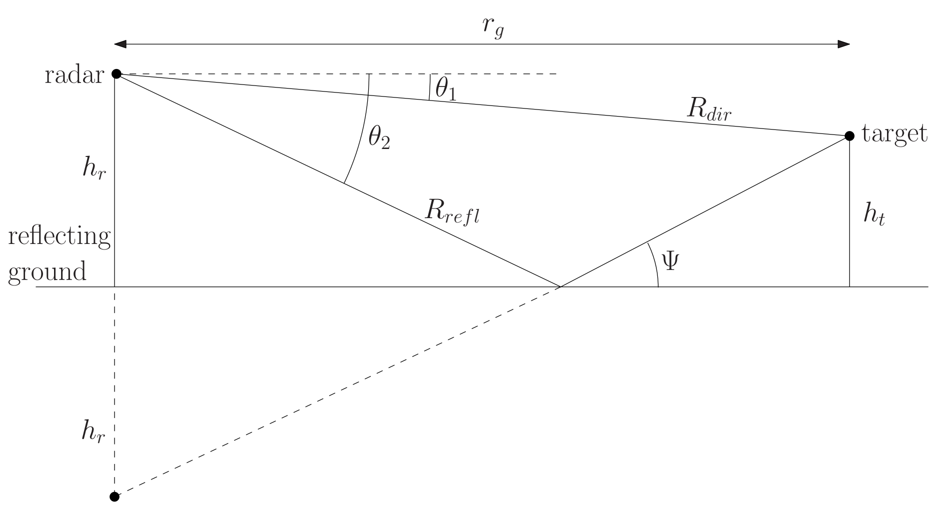

Figure A.1: *Flat-earth model for ground multipath.*

The delay δ between the reflected and direct paths can be estimated as

$$\begin{aligned} \delta &= \frac{R_{refl} - R_{dir}}{c} \\ &= \frac{1}{c}\left(\sqrt{(h_r + h_t)^2 + r_g^2} - \sqrt{(h_r - h_t)^2 + r_g^2}\right) \qquad \text{(A.1)} \\ &\leq 1\text{ns}, \end{aligned}$$

Table A.1: *Targets relative height as measured by the Leica TS15 Total Station.*

Target	h_t (m)	$h_t - h_r$ (m)
P1	99.9910	-0.8680
P2	100.0233	-0.8380
P3	100.0833	-0.7780
P3, lower height	99.5307	-1.3280
P4	100.1721	-0.6880
radar	100.8580	0

which is much less than the 100 μs width of the radar pulse. We can thus assume that the reflected and direct path pulses interfere at the location of the target. The delay δ is also less than the 3 ns resolution of the radar ($\Delta t = c/2B$ where B is the 150 MHz bandwidth of the radar), hence the different multipath signals are not resolved by the radar.

Assuming that $h_r, h_t \ll R$, and $\theta_1 \simeq \theta_2 = \theta$, we can use the following formula for the propagation factor F[22]:

$$F = f(\theta) \left| \sqrt{1 + \rho^2 - 2\rho \cos\left(\phi + \frac{2\pi\delta}{\lambda}\right)} \right| \tag{A.2}$$

where $\Gamma = \rho e^{-i\phi}$ is the complex reflection coefficient of amplitude ρ and phase ϕ, λ is the wavelength and $f(\theta)$ is the antenna pattern effect. $f(\theta)$ can be set equal to 1 in our case.

The complex reflection coefficient for vertical polarization can be determined using the following formula [23]:

$$\Gamma_V = \frac{\epsilon \sin\Psi - \sqrt{\epsilon - (\cos\Psi)^2}}{\epsilon \sin\Psi + \sqrt{\epsilon - (\cos\Psi)^2}} \tag{A.3}$$

where $\epsilon = \epsilon' - i\epsilon''$ is the complex dielectric constant. Reported values for the complex dielectric constant of snow at 9 GHz range between 1.15 and 2.6 for ϵ' and between 0.1 and 0.95 for ϵ'' depending on the water content and density of snow [24]. The reflection coefficient around 6° grazing angle converges to 0.64 for the magnitude and 178° for the phase for most of the reported dielectric constant values. We use these values in what follows.

In Figure A.2 is shown the propagation factor F^2 on a logarithmic scale as a function of the target height relative to the radar height, for an assumed radar height of 2.35 m. The propagation factor is plotted for both a smooth surface and surface with roughness factor of 0.7. We see that the propagation factor can take values between +4.3 dB for constructive interference and -8.8 dB for destructive interference for the smooth surface, or between +3.2 dB and -5.1 dB for the rough surface. Note that the propagation factor F^2 appears in the one-way radar range equation, and that F^4 appears in the two-way radar range equation. The propagation factor can thus easily explain some 7 dB difference between the same target at two different heights (scenes 2 and 3 of our experimental data).

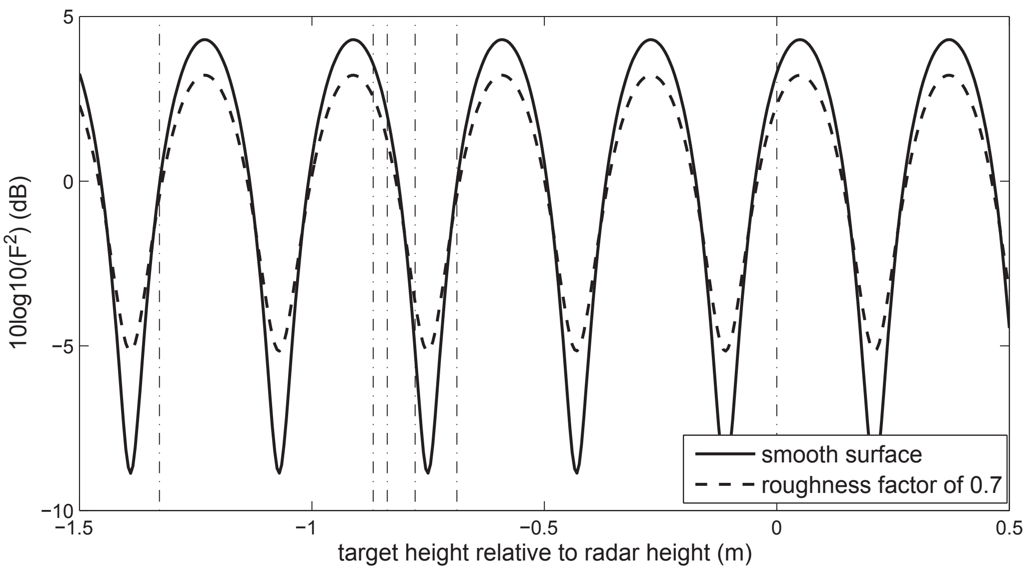

Figure A.2: *Propagation factor as a function of target height relative to radar height.*

In fact, the dashed vertical lines of Figure A.2 indicate the heights of the different targets and the radar. Note that we do not know exactly the height of the radar relative to the height of the reflection point on the ground, so the dashed lines on the Figure could be shifted relative to the propagation factor curve. Nonetheless, using our best guess of radar height of 2.35 m and the snow dielectric constant, we can tabulate the predicted values for the propagation factor in the two-way radar equation. Table A.2 compares the predicted values with the relative power of the targets from Figure 13. There is a fairly good agreement between the simple model and the experimental results, except for the target at 15° azimuth. But recall that this target is losing an extra 6 dB due to the azimuth antenna beamwidth. The predictions with a smooth surface exacerbate the difference in power levels, where the predictions using a rough surface better compare with the experimental results.

Table A.2: *Power levels predicted by the simple flat earth model and observed in the experimental data.*

Target	Observed relative power (dB)	Predicted two-way propagation factor smooth surface (dB)	rough surface (dB)
P1	44.9	7.1	5.1
P2	43.3	4.0	2.5
P3	33.8	−10.3	−7.4
P3, lower height	40.0	−0.2	−1.0
P4	33.0	−0.1	−0.9

DOCUMENT CONTROL DATA

(Security markings for the title, abstract and indexing annotation must be entered when the document is Classified or Protected.)

1. ORIGINATOR (The name and address of the organization preparing the document. Organizations for whom the document was prepared, e.g. Centre sponsoring a contractor's report, or tasking agency, are entered in section 8.) DRDC – Ottawa Research Centre 3701 Carling Avenue, Ottawa ON K1A 0Z4, Canada	2a. SECURITY MARKING (Overall security marking of the document, including supplemental markings if applicable.) UNCLASSIFIED 2b. CONTROLLED GOODS (NON-CONTROLLED GOODS) DMC A REVIEW: GCEC DECEMBER 2012

3. TITLE (The complete document title as indicated on the title page. Its classification should be indicated by the appropriate abbreviation (S, C or U) in parentheses after the title.)

Experimental verification of multiple-input multiple output (MIMO) beamforming capabilities using a time-division coherent MIMO radar

4. AUTHORS (Last name, followed by initials – ranks, titles, etc. not to be used.)

Sévigny, P.; Moo, P. W.; Laneve, T.

5. DATE OF PUBLICATION (Month and year of publication of document.)	6a. NO. OF PAGES (Total containing information. Include Annexes, Appendices, etc.)	6b. NO. OF REFS (Total cited in document.)
April 2015	58	24

7. DESCRIPTIVE NOTES (The category of the document, e.g. technical report, technical note or memorandum. If appropriate, enter the type of report, e.g. interim, progress, summary, annual or final. Give the inclusive dates when a specific reporting period is covered.)

Scientific Report

8. SPONSORING ACTIVITY (The name of the department project office or laboratory sponsoring the research and development – include address.)

DRDC – Ottawa Research Centre
3701 Carling Avenue, Ottawa ON K1A 0Z4, Canada

9a. PROJECT OR GRANT NO. (If appropriate, the applicable research and development project or grant number under which the document was written. Please specify whether project or grant.)	9b. CONTRACT NO. (If appropriate, the applicable number under which the document was written.)
10a. ORIGINATOR'S DOCUMENT NUMBER (The official document number by which the document is identified by the originating activity. This number must be unique to this document.) DRDC-RDDC-2015-R051	10b. OTHER DOCUMENT NO(s). (Any other numbers which may be assigned this document either by the originator or by the sponsor.)

11. DOCUMENT AVAILABILITY (Any limitations on further dissemination of the document, other than those imposed by security classification.)

Unlimited

12. DOCUMENT ANNOUNCEMENT (Any limitation to the bibliographic announcement of this document. This will normally correspond to the Document Availability (11). However, where further distribution (beyond the audience specified in (11)) is possible, a wider announcement audience may be selected.)

Unlimited

13. ABSTRACT (A brief and factual summary of the document. It may also appear elsewhere in the body of the document itself. It is highly desirable that the abstract of classified documents be unclassified. Each paragraph of the abstract shall begin with an indication of the security classification of the information in the paragraph (unless the document itself is unclassified) represented as (S), (C), or (U). It is not necessary to include here abstracts in both official languages unless the text is bilingual.)

Recently, there has been increasing interest from the research community in multiple-input multiple output (MIMO) architectures for a variety of radar applications. We are interested in clarifying the angle estimation accuracy of coherent or co-located MIMO radar to gain an accurate understanding of its potential benefits. The theoretical two-way antenna radiation patterns are derived for three configurations of a linear array: a phased array configuration, a MIMO-1 configuration using orthogonal waveform transmission on all elements, and a MIMO-2 configuration using orthogonal waveform transmission on the two end elements. Field experimental results obtained with an 8-element X-band linear array time-division radar and trihedral targets are discussed. Phased array radar data obtained with a Mixed Experiments and Simulations Approach (MESA) are also discussed. It is found that the experimental mainbeam patterns match the theoretical patterns. MIMO-1 is shown to have the same two-way radiation pattern as that of a phased array radar configuration. Compared to MIMO-1 and phased array, MIMO-2 has enhanced angle estimation accuracy, lower gain and higher sidelobes, while only requiring two orthogonal waveforms on transmit.

14. KEYWORDS, DESCRIPTORS or IDENTIFIERS (Technically meaningful terms or short phrases that characterize a document and could be helpful in cataloguing the document. They should be selected so that no security classification is required. Identifiers, such as equipment model designation, trade name, military project code name, geographic location may also be included. If possible keywords should be selected from a published thesaurus. e.g. Thesaurus of Engineering and Scientific Terms (TEST) and that thesaurus identified. If it is not possible to select indexing terms which are Unclassified, the classification of each should be indicated as with the title.)

Multiple-input multiple output (MIMO) radar, phased array radar, antenna radiation pattern

DRDC | RDDC

SCIENCE, TECHNOLOGY AND KNOWLEDGE FOR CANADA'S DEFENCE AND SECURITY | SCIENCE, TECHNOLOGIE ET SAVOIR POUR LA DÉFENSE ET LA SÉCURITÉ DU CANADA

www.drdc-rddc.gc.ca